Strain-Based Shape and 3-D Force Estimation for Rod-Driven Continuum Robots With Stretch Sensors

Peiyi Wang, *Member, IEEE*, Daniel Feliu-Talegon, *Member, IEEE*, Yuchen Sun, Zhexin Xie, *Member, IEEE*, Wenci Xin, *Member, IEEE*, Muhammad Sunny Nazeer, *Member, IEEE*, Cosimo Della Santina, *Senior Member, IEEE*, Cecilia Laschi, *Fellow, IEEE*, and Federico Renda, *Member, IEEE*

***Abstract*—Soft robots' ability to safely navigate complex environments motivates the development of algorithms for accurate environmental interaction assessment, enabling greater autonomy. Specifically, strain-based shape and force estimation of continuum robots with embedded soft sensors poses an open challenge mainly owing to continuous softness, anisotropic deformation, and nonlinear properties. Mathematical description of deformable soft bodies and accurate estimation of external forces are crucial for achieving controllable and intelligent behaviors of these robots. In this article, a kinetostatic strain-based modeling for rod-driven soft robots with embedded stretch sensors is proposed, which incorporates local strains, actuation variables, and external interactions. The strain model enables full shape estimation of the robot and prediction of strain variations in soft bodies. Building on this, we develop a force estimator based on predicted and measured sensor and actuator lengths to evaluate 3-D external forces, accounting for both orthogonal and tangential components relative to the backbone. Moreover, we introduce a methodology using a novel ellipsoid representation to handle tangential forces that may become insensitive in certain singular configurations. This estimator allows us to either disregard such forces when they do not influence deformation or estimate them when they become observable. Our simulations and experiments demonstrate how this approach can be used to analyze the robot's configuration and successfully estimate external forces. Finally, it is demonstrated that when the continuum arm follows trajectories with higher strain sensitivity, tangential force estimation is significantly improved.**

***Index Terms*—Continuum mechanics, force and shape estimation, physical interaction, Soft continuum robot, stretch sensor.**

Received 6 November 2025; accepted 19 December 2025. Date of publication 14 January 2026; date of current version 2 February 2026. This work was supported in part by the National Research Foundation, Singapore, under its Medium Sized Centre Programme - Centre for Advanced Robotics Technology Innovation (CARTIN), and NUS Start-up Grant "RoboLife," in part by the US Office of Naval Research Global under Grant N62909-21-1-2033, in part by Khalifa University under Grant RIG-2023-048 and Grant RC1-2018-KUCARS, in part by the European Union (ERC, RIPLEY, 101165078), in part by National Research Foundation, Prime Minister's Office, Singapore under its Campus for Research Excellence and Technological Enterprise programme. This article was recommended for publication by Associate Editor P. Renaud and Editor H. Zhao upon evaluation of the reviewers' comments. *(Peiyi Wang and Daniel Feliu-Talegon contributed equally.) (Corresponding author: Peiyi Wang.)*

Peiyi Wang and Wenci Xin are with the Singapore MIT Alliance for Research and Technology (SMART) centre, Singapore, and also with the Department of Mechanical Engineering, National University of Singapore, Singapore 117575 (e-mail: peiyi.wang@smart.mit.edu; wenci.xin@smart.mit.edu, wxin@u.nus.edu).

Daniel Feliu-Talegon and Cosimo Della Santina are with the Cognitive Robotics Department, Delft University of Technology, 2628 Delft, The Netherlands (e-mail: d.feliutalegon@tudelft.nl; C.DellaSantina@tudelft.nl).

Yuchen Sun, Muhammad Sunny Nazeer, and Cecilia Laschi are with the Department of Mechanical Engineering, National University of Singapore, Singapore 117575, and also with the Department of Mechanical Engineering and Advanced Robotics Centre, National University of Singapore, Singapore 117575 (e-mail: sun.yuchen22@u.nus.edu; m.nazeer@nus.edu.sg; mpeclc@nus.edu.sg).

Zhexin Xie is with the Department of Mechanical and Energy Engineering, Southern University of Science and Technology, Shenzhen 518055, China (e-mail: xiezx@sustech.edu.cn).

Federico Renda is with the Khalifa University Center for Autonomous Robotics System (KUCARS), Abu Dhabi 127788, UAE, and also with the Department of Mechanical and Nuclear Engineering, Khalifa University of Science and Technology, Abu Dhabi 127788, UAE (e-mail: federico.renda@ku.ac.ae).

This article has supplementary downloadable material available at https://doi.org/10.1109/TRO.2026.3653859, provided by the authors.

Digital Object Identifier 10.1109/TRO.2026.3653859

I. Introduction

Soft continuum robots, built from elastomeric materials, are distinguished by their high degrees of freedom and inherent softness, offering unprecedented flexibility and adaptability for a wide range of applications such as surgery, rehabilitation, and elderly care [1], [2]. Among these, the most commonly used actuations embedded inside the soft body includes tendons [3], [4], flexible rods [5], and fluid chambers [6], [7]. Although they provide precise and stable length or pressure feedback, the entire shape varies in response to any input from environmental interactions [8]. Typically, actuation feedback alone cannot accurately capture real-time shape deformations and estimate external forces. However, soft robot with embedded sensors [9], [10], [11], [12], unlike expensive and bulky tracking devices such as electromagnetic tracking, RGB-D camera, or motion capture systems, is a compact and effective way to address this challenge.

Although mathematical models predict the deformable soft body, given actuator lengths and external disturbances, some unexpected interactions applied to the robot will cause a significant mismatch between the predicted shape and the sensed shape [13], [14]. Perception methods based on colocated stretch sensors [10] play a similar role in simultaneously evaluating the shape and external force conditions among continuum robots, just as joint encoders and force/torque sensors do among rigid-link robots. To achieve this goal, an accurate mathematical model of the deformable and sensorized soft body is required. For slender continuum robots, due to the anisotropic stiffness, especially the axial stiffness is much higher than the bending stiffness, some configurations may lead to situations where

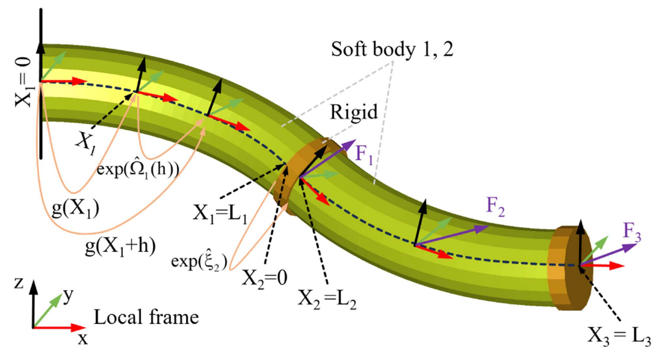

Fig. 1. Detailed schematic of the GVS model illustrating the recursive formulation of the kinematic of the robot $g_i(X_i)$.

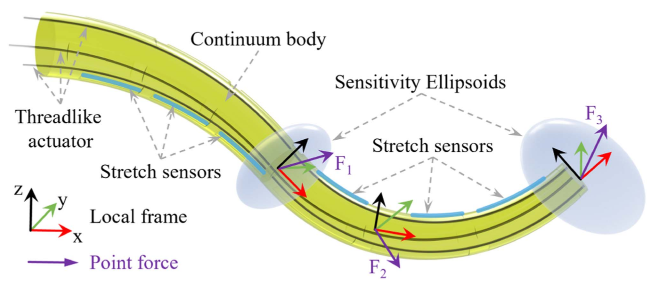

Fig. 2. Detailed schematic of the strain-based shape and force estimation. The continuum robot consists of soft body, stretch sensors, and threadlike actuator. Visualizing the ellipsoids at any force point along the soft body.

the embedded strain sensor is insensitive to certain interaction forces. [11], [15], [16], [17], [18]. To avoid such singularity and insensitivity, it is necessary to explore methods that identify potential insensitive directions and adjusts the configuration to enable to estimate interaction forces

This article extends the preliminary work presented in [19], with a focus on introducing the GVS approach for estimating the rod-driven soft robots (RDSRs) shape and sensor length. The current work offers substantial improvements including strain-based shape & 3-D force estimation and visualization ellipsoid. The schematic of the strain method and sensitivity ellipsoid is illustrated in Figs. 1 and 2. Specifically, visualization ellipsoids are constructed at the applied force points to determine if the strain sensor is sensitive to the tangential force component. The force estimator can then evaluate these forces when they are observable through the local strain. In addition, the simulation and experimental analysis in the sensorized RDSR, composed of soft body, embedded with eGaIn-based strain sensors and driven by flexible rods (see Section V and Fig. 3 for more details), demonstrate the functionality of the proposed estimation method and the working principle of the visualization ellipsoid. In this study, the location of the external force is known to the force estimator, so its estimation is not our focus. The main contributions are summarized as follows.

1) We develop a strain-based method incorporating local strains, internal actions, and external interactions for simultaneous estimation of 3-D force and shape in rod-driven continuum robots with embedded stretch sensors.

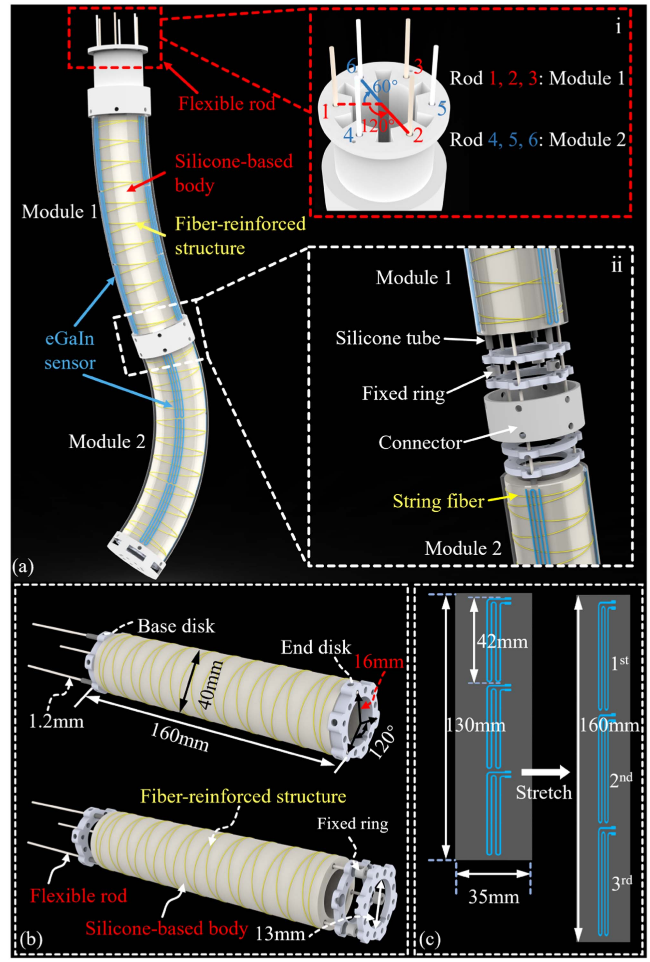

Fig. 3. Rod-driven soft robot (RDSR) with embedded strain sensors. (a) Assembly and design of the whole arm with soft sensors embedded on the surface: (i) Positions of actuation rods in modules 1 and 2 and (ii) detailed structure of connector between each module. (b) Structure of one-module RDSR. (c) Initial and stretched state of a liquid metal eutectic gallium-indium (eGaIn)-based PSS.

2) We propose a method to identify configurations in which forces along the backbone direction produce negligible strain responses, making them difficult to estimate. To address this, we introduce a new ellipsoid that illustrates the sensitivity of strains to external forces applied along the backbone and other directions. Then, we can decide whether to neglect this component of the force, since it has little impact on the robot's shape, or to change the configuration in order to successfully estimate it.
3) The functionality of shape and 3-D force estimation (including tangential and orthogonal forces), as well as the working principles of the visualized ellipsoid and strain-based sensitivity, are validated and demonstrated via simulations and experiments.

The rest of this article is organized as follows: Section II is devoted to the related work. In Section III, we introduce the necessary elements of the GVS model and formulate the static equations. Section IV proposes the strain-based estimation method and calculates sensitivity ellipsoids. The robotic prototype and system are introduced and described in Section V. Then, the strain sensitivity is defined and analyzed through model simulation in Section VI. Section VII validate and demonstrate the feasibility and reliability of shape and force estimation, and the functionality of the visualization ellipsoid and strain sensitivity. Finally, Section VIII concludes this article.

II. Related Work

This section describes existing methods for modeling the deformation characteristics of soft continuum robots, estimating external forces, and using ellipsoids to analyze their behavior.

A. Mathematical Modeling

For deformable soft bodies, purely geometric assumptions such as constant curvature (CC) model [20], piecewise constant curvature model [21], and variable curvature [22] commonly ignore several important factors such as gravity, friction, and environmental interactions, despite they enable proprioception and disturbance observation of soft arms [9], [23], [24] by embedding colocated sensors in the corresponding segments to estimate shape parameters. However, theoretical models must include geometric parameters such as actuation variables as well as physical parameters such as material elasticity and internal and external interactions to fully consider all deformations in soft materials [8], [13], especially when operating in unstructured environments [25].

All degrees of freedom (DOFs) of all topologies required for soft robots can be described using 3-D continuum solid mechanics such as finite-element method (FEM) and Cosserat rod model. FEM with meshed elements provides a set of discrete equations for statics and differential equations for dynamics. The convergent solution is severely limited by the element number, mesh quality, and boundary constraints and requires extensive computational sources. Therefore, modal reduction and equivalent simplification are essential to achieve a balance between good accuracy and high-speed calculation in robot control [26]. The Cosserat rod theory is commonly used in tendon-driven continuum robots [27], [28], concentric tube continuum robots [29], multibackbone continuum robots [30], [31], and pneumatic soft robots [27] for modeling the statics and dynamics of these systems. A shooting-based algorithm and an implicit time-integration scheme were proposed to solve the spatial boundary value problem of the Cosserat rod equations, but the root-finding process of convergent solutions is time consuming and it has been shown to be much more fragile and unstable when the time step decreases below a critical value [32], [33]. An alternative method for modeling Cosserat rods is referred to as geometric variable strain (GVS) approach [34], [35], developing a series of explicit recursive formulas by discretizing the continuous soft body into a finite set of strain basis functions. Such parameterized strain plays the same role as that of the DOFs in traditional robotics. In this way, soft robots, rigid robots, and hybrids of both can be described by the generalized GVS [33], such as the CC model for continuum robots [20] and joint-based modeling of rigid robots [36]. The GVS-based model demonstrated general applicability and good performance in terms of accuracy and complexity for tendon-driven, fluid-driven, and concentric tube continuum robots [34], [37], [38]. Benefiting from the explicit approximation of kinematic formulas, geometric Jacobian, and actuation matrix of soft robots, real-time static and dynamic model-based control is feasible in this field [39], [40]. More importantly, these models are generic and can accommodate discontinuities in the strain field, thus providing more flexibility in their parameterization and enabling feasibility for integration with sensorized strains. Overall, the discrete strain model still needs further exploration in the soft continuum robot with local strain sensors, actuators, and an optimal number of DOFs [19]. Initial attempts to combine the GVS approach with actuation sensor readings demonstrated its effectiveness in perceiving the robot's shape and external tip forces [41].

B. Force Estimation

Regarding force estimation, direct tactile sensors provide feedback on contact conditions of the corresponding area [42], [43], [44], [45], but more sensors need to be installed at specific locations and directions of interest.

The perception method that combines mathematical models and sensory systems is an efficient and common way to estimate external forces. "Intrinsic wrench sensing" was proposed by using an actuation-based sensing algorithm derived from the CC model and the principle of virtual work [46], [47]. Still, it is difficult to capture the interaction position using only the actuation load sensor. Deflection-based force sensing explored a combination of Gaussian process regression or extended Kalman filter with the Cosserat rod model to estimate point and distributed forces [15], [16], [17]. Curvature obtained by wrapped fiber Bragg grating (FBG) was merged into the theoretical model to implement shape proprioception and real-time force estimation [18], [48], [49], [50]. However, due to the high axial stiffness relative to the bending stiffness of slender continuum robots [49], they face ill-conditioning problems of estimating force in certain configurations when using deflection-based and curvature-based sensing methods. Prior works made a strong assumption that the applied force is orthogonal to the robot backbone curve [16], [17], [18]. In fact, applying these assumptions in theoretical models and experimental scenarios is not always true and suitable. In this context, Feliu-Talegon et al. [51] propose an efficient methodology for estimating 3-D forces using only tendon actuation readings, demonstrating that estimating forces along the backbone in some configurations is particularly challenging. Redundant configurations in soft continuum robots may result in situations where strain sensors are insensitive to certain interaction forces, as occurs in the articulated robot [52]. If the robot reaches a configuration where the local strain sensor cannot observe certain external forces, which will result in unexpected interactions and damages. Therefore, these insensitive situations and unobservable singularities should be deeply analyzed and avoided in critical applications and real scenarios. Understanding and correctly estimating forces tangential to the backbone when the aforementioned assumption is not applicable remains an open question in this field.

C. Visualized Ellipsoids

The famous concept of manipulability and compliance ellipsoids has been greatly developed since its first introduction by Yoshikawa [53], resulting in different calculation methods, analyses, and applications. Manipulability ellipsoids are easy to compute in rigid-link manipulators and act as powerful and intuitive descriptors to analyze and control the robot's dexterity. Different ellipsoid descriptors can be optimized according to task requirements, such as tracking a desired trajectory while applying a specific force [54], [55]. Combined with position control, Wong et al. [52] introduce a novel sensor observability ellipsoid to monitor the force detection capability of redundant rigid manipulators based on joint torque sensors. Different observability of different joint configurations are obtained in real time to optimize the maximum observation of external forces. Manipulability analysis has also been extended to continuum robots very early on. Gravagne and Walker [56] demonstrated the variations in manipulability and compliance ellipsoid from a single-actuator to multiactuator manipulator based on inextensible kinematic model. Smoljkic et al. [57] presented a method to calculate the compliance and its ellipsoid by using the forward kinematic coupling solution in a nonactuated elastic tube. Bamdad et al. [58] calculated a manipulability index beside the reachability map based on a kinematics model to evaluate the effectiveness of continuation analysis for granular soft manipulators. Ma et al. [59] analyzed the dexterity and manipulability of a continuum robot considering multiple obstacles in confined spaces. Constructing manipulability and compliance ellipsoids of soft continuum robots based on the Cosserat rod theory is still an active research problem [60], [61], [62], and using visualized ellipsoids to analyze strain-based sensitivity in response to external forces presents an additional challenge. To the best of the authors' knowledge, current studies have not yet explored in depth theoretically the mapping relationship between external forces and perceived local strains and its visualization ellipsoid in the field of soft continuum robotics.

III. GVS Model

We outline the fundamental elements of the GVS model and provide the static equilibrium equations applicable to the continuum robot under investigation. For detailed static modeling, the reader is referred to [34].

A. Robot Kinematics

The configuration of a slender soft body i can be modeled as a continuous stack of rigid cross-sections parameterized by a curvilinear abscissa $X_i \in [0, L_i]$, where L_i is the length of the rod i (see Fig. 1). The configuration of a link can be represented by defining a homogeneous transformation matrix along the curvilinear abscissa. This matrix represents a coordinate frame attached to the cross sections of the link and is defined as the following spatial curve:

$$\boldsymbol{g}_i(X_i) = \begin{bmatrix} \boldsymbol{R}_i(X_i) & \boldsymbol{r}_i(X_i) \\ \boldsymbol{0} & 1 \end{bmatrix} \in \mathrm{SE}(3) \tag{1}$$

where $\boldsymbol{r}_i(X_i) \in \mathbb{R}^3$ is the position of the local frame, while $\boldsymbol{R}_i(X_i) \in \mathrm{SO}(3)$ provides the orientation of the local frame relative to the spatial frame. We can differentiate the configuration of the system with respect to X $(\cdot)'$ and t $\dot{(\cdot)}$ obtaining

$$\boldsymbol{g}_i'(X_i) = \boldsymbol{g}_i \hat{\boldsymbol{\xi}}_i(X_i), \qquad \dot{\boldsymbol{g}}_i(X_i) = \boldsymbol{g}_i \hat{\boldsymbol{\eta}}_i(X_i) \tag{2}$$

where $\hat{(\bullet)}$ denotes the isomorphism between $\mathbb{R}^6$ and se(3). The previous partial derivatives have been expressed in terms of the twists defined in the local frame of the system at X_i, where the strain $\hat{\boldsymbol{\xi}}_i$ and velocity $\hat{\boldsymbol{\eta}}_i$ twists of the body are defined. Spatial integration of the left-hand side of (2) yields

$$\boldsymbol{g}_i(X_i) = \boldsymbol{g}_i(0) \exp\left(\widehat{\boldsymbol{\Omega}}_i(X_i)\right) \tag{3}$$

where $\boldsymbol{\Omega}_i(X_i)$ is the Magnus expansion of $\boldsymbol{\xi}_i(X_i)$. The exponential map in SE(3) and the Lie algebra associated with a Lie group used in this section can be found in [63]. The soft links are divided into smaller intervals of lengths h_j and $\boldsymbol{g}_i(X_i)$ is computed recursively through these intervals

$$\boldsymbol{g}_i(X_i + h_j) = \boldsymbol{g}_i(X_i) \exp\left(\widehat{\boldsymbol{\Omega}}_i(h_j)\right) . \tag{4}$$

For the case of a rigid link/joint i the configuration is divided in two: the initial configuration $X_i = 0$, and the final $X_i = L_i$

$$\boldsymbol{g}_i(L_i) = \boldsymbol{g}_i(0) \exp\left(\widehat{\boldsymbol{\xi}}_i\right) \tag{5}$$

where $\widehat{\boldsymbol{\xi}}_i$ for rigid transformation is constant.

B. Differential Kinematics

The relation between screw strain and velocity is established through the equality of the mixed partial derivatives in space and time

$$\boldsymbol{\eta}_i'(X_i) = \dot{\boldsymbol{\xi}}_i(X_i) - \mathrm{ad}_{\boldsymbol{\xi}_i(X_i)} \boldsymbol{\eta}_i(X_i) \tag{6}$$

where $\mathrm{ad}_{(\bullet)} \in \mathbb{R}^{6\times 6}$ is the adjoint operator of se(3). By virtue of the identity $(\mathrm{Ad}_{\boldsymbol{g}_i})' = \mathrm{Ad}_{\boldsymbol{g}_i} \mathrm{ad}_{\boldsymbol{\xi}_i}$ and the Leibniz rule for the derivative of a product, it can be verified that the analytic solution of (6) is given by

$$\boldsymbol{\eta}_i(X_i) = \mathrm{Ad}_{\boldsymbol{g}_i^{-1}(X_i)} \int_0^{X_i} \mathrm{Ad}_{\boldsymbol{g}_i(X_i)} \dot{\boldsymbol{\xi}}_i(X_i) ds \tag{7}$$

where $\mathrm{Ad}_{\boldsymbol{g}_i}$ is the adjoint representation of $\boldsymbol{g}_i$.

The strain field $\boldsymbol{\xi}_i$ can be discretized by choosing a specific set of vector functions to serve as a finite basis for the field. This can be represented as

$$\boldsymbol{\xi}_i(X_i) = \boldsymbol{\Phi}_{\xi_i}(X_i)\boldsymbol{q} + \boldsymbol{\xi}_i^*(X_i) \tag{8}$$

where $\boldsymbol{\Phi}_{\xi_i}(X_i) \in \mathbb{R}^{6\times n}$ is the matrix function whose columns form the basis for the strain field, $\boldsymbol{q} \in \mathbb{R}^n$, n being the DOFs, is the vector of generalized coordinates for the chosen basis function. Equation (8) can be substituted into (6), eventually leading to the definition of geometric Jacobian

$$\boldsymbol{\eta}_i(X_i) = \mathrm{Ad}^{-1}_{\boldsymbol{g}_i(X_i)} \int_0^{X_i} \mathrm{Ad}_{\boldsymbol{g}_i(X_i)} \boldsymbol{\Phi}_{\xi_i} ds \dot{\boldsymbol{q}} = \boldsymbol{J}_i(\boldsymbol{q}, X_i)\dot{\boldsymbol{q}}. \tag{9}$$

Although (3) and (9) are analytical expressions, for a general variable strain case, they cannot be computed explicitly. The GVS approach employs a finite set of strain bases to discretize the continuous strain field in intervals. In this work, we use the fourth-order Zanna collocation approach with a two-stage Gauss quadrature as detailed in [64].

C. Statics Equations Including Internal and External Forces

The discrete model that represents the static equilibrium of our system can be obtained by projecting the equilibrium equations by means of the D'Alembert Principle [19]

$$\boldsymbol{K}\boldsymbol{q} = \boldsymbol{B}\left(\boldsymbol{q}\right)\boldsymbol{u} + \boldsymbol{Q}_e(\boldsymbol{q}) \tag{10}$$

where $\boldsymbol{K} \in \mathbb{R}^{n\times n}$ is the generalized internal elastic force, $\boldsymbol{Q}_e(\boldsymbol{q}) \in \mathbb{R}^n$ is the vector of generalized external forces, $\boldsymbol{B}(\boldsymbol{q}) \in \mathbb{R}^{n\times n_a}$ is the generalized actuation matrix being n_a the number of actuators, and $\boldsymbol{u}$ is the vector of applied actuation forces. We propose to use a Hooklike linear elastic law to describe the rod elasticity, then the internal elastic force matrix can be expressed as

$$\boldsymbol{K} = \mathrm{diag}_{i=1}^{N}\left(\int_0^{L_i} \boldsymbol{\Phi}_{\xi_i}^T(X_i)\boldsymbol{\Sigma}_i(X_i)\boldsymbol{\Phi}_{\xi_i}(X_i)dX_i\right) \tag{11}$$

where $\boldsymbol{\Sigma}_i$ is the screw elasticity matrix of a cross section. The generalized actuation force considers a Cosserat rod internally actuated by several threadlike actuators similar to cables, rods, or fluidic actuation [34]. Then, the actuation wrench can be obtained by computing the force and moment exerted by the internal actuator on the midline of the robot. This is given by

$$\boldsymbol{\mathcal{F}}_{a_i}(X_i) = \sum_{k=1}^{n_{a_i}} \begin{bmatrix} \tilde{\boldsymbol{d}}_{ik}\boldsymbol{t}_{ik} \\ \boldsymbol{t}_{ik} \end{bmatrix} u_{ik} = \boldsymbol{\Phi}_{a_i}(\boldsymbol{q}, X)\boldsymbol{u}_i \tag{12}$$

where $\boldsymbol{\Phi}_{a_i}(\boldsymbol{q}, X) \in \mathbb{R}^{6\times n_{a_i}}$ is the actuation basis in the element i, n_a is the number of actuators, $\boldsymbol{d}_{ik}(X_i) \in \mathbb{R}^3$ is the distance from the midline to actuator k, $\boldsymbol{t}_{ik}(X_i) \in \mathbb{R}^3$ is the unit vector tangent to the actuator's path, $\boldsymbol{u}_i$ is the magnitude of the actuation force, and $\tilde{\bullet}$ is the skew-symmetric matrix representation of so(3). Then, the generalized internal actuation can be obtained via D'Alembert's principle as follows:

$$\boldsymbol{B}\left(\boldsymbol{q}\right)\boldsymbol{u} = ||_{i=1}^{N}\left(\int_0^{L_i} \boldsymbol{\Phi}_{\xi_i}^T\boldsymbol{\Phi}_{a_i}dX\right)\boldsymbol{u} \tag{13}$$

where $||$ is the vector concatenation operator.

Finally, the vector of generalized external forces can be expressed as

$$\boldsymbol{Q}_e(\boldsymbol{q}) = \sum_{i=1}^{N}\int_0^{L} \boldsymbol{J}_i^T\overline{\boldsymbol{\mathcal{M}}}\mathrm{Ad}_{\boldsymbol{g}}^{-1}\boldsymbol{G}dX + \sum_{k=1}^{n_p}\boldsymbol{J}_k^T\mathrm{Ad}^*_{\boldsymbol{g}_{\theta_k}^{-1}}\boldsymbol{\mathcal{F}}_k \tag{14}$$

where N is the total number of links, n_p is the number of external point wrench, $\boldsymbol{\Sigma}$ is the screw elasticity matrix of a cross section, $\overline{\boldsymbol{\mathcal{M}}}\mathrm{Ad}_{\boldsymbol{g}_{\theta_i}}^{-1}\boldsymbol{G}$ is the distributed external force due to gravity, $\overline{\boldsymbol{\mathcal{M}}} = \rho\mathrm{diag}(J_x, J_y, J_z, A, A, A)$ is the screw inertia density matrix of the cross section (ρ is the density, A is the cross-section area, and $J_\bullet$ is the second moment of area), $\boldsymbol{g}_{\theta_k}$ is the rotational component of $\boldsymbol{g}_i$ at the position where the wrench $\boldsymbol{\mathcal{F}}_k$ is applied, $\boldsymbol{G} = [\boldsymbol{0}^T\boldsymbol{a}_g^T]^T$, where $\boldsymbol{a}_g$ is the acceleration due to gravity in the global frame, and $\boldsymbol{\mathcal{F}}_k = [\boldsymbol{M}_k^T\ \boldsymbol{F}_k^T]^T$ is the external point wrench, expressed in the global frame, with the moment and force components separated. We use the coadjoint map of SE(3), denoted as $\mathrm{Ad}^*_{\boldsymbol{g}}$, which transforms wrenches from the local frame to the global frame. In our case where $\boldsymbol{g}_{\theta_k}$ is only the rotational component, we have that

$$\mathrm{Ad}^*_{\boldsymbol{g}_{\theta_k}^{-1}} = \begin{pmatrix} \boldsymbol{R}_k^T & \boldsymbol{0}_{3\times 3} \\ \boldsymbol{0}_{3\times 3} & \boldsymbol{R}_k^T \end{pmatrix} \in \mathbb{R}^{6\times 6}.$$

Similar to $\boldsymbol{g}_i$, the geometric Jacobian $\boldsymbol{J}_i$ is recursively computed using the approximated form of Magnus expansion. For more comprehensive details, readers may refer to [33], where the static and dynamic analysis of soft-rigid hybrid robots with multidimensional rigid joints is discussed. This reference also includes the derivation of the key equations described in the proposed model.

IV. Shape and Force Estimation Method

In this section, we propose a shape and force estimation method for continuum robots that are internally actuated using threadlike actuators. The method employs stretch sensors placed at different parts of the robot to infer body deformation and utilizes the kinetostatic strain-based modeling described in Section III, together with the actuation inputs, to simultaneously estimate the shape and external force. Fig. 2 presents the detailed schematic of the estimation method for continuum robots with threadlike actuators (such as cables, flexible rods, or pneumatic chambers) and stretch sensors.

A. Length Kinematic Equation

The change in length of a threadlike actuator, k, embedded inside a soft manipulator can be mathematically calculated by integrating along the segment of the body where the actuator is embedded, denoted by the interval $[a_i,\ b_i]$, with $0 \leq a_i, b_i \leq L_i$ as developed in [64]. This variation can then be computed as a function of the shape of the soft robot and the routing of the threadlike actuator inside the robot as follows:

$$y_k = \left(\int_{a_i}^{b_i} \boldsymbol{\Phi}_{a_k}^T\boldsymbol{\Phi}_{\boldsymbol{\xi}_i}dX\right)\boldsymbol{q} + \int_{a_i}^{b_i}(\boldsymbol{\Phi}_{ak} - \boldsymbol{\Phi}^*_{ak})^T \times \left(\boldsymbol{\xi}^* - \begin{bmatrix}\boldsymbol{0} \\ \boldsymbol{d}'_k\end{bmatrix}\right)dX. \tag{15}$$

The aforementioned equation can be represented in matrix form by gathering the change in length for multiple actuators

$$\boldsymbol{y} = \boldsymbol{B}(\boldsymbol{q})^T\boldsymbol{q} + \boldsymbol{z}(\boldsymbol{q}). \tag{16}$$

Moreover, [64] also derives the derivative of the previous expression, yielding

$$dy_k = \int_{a_i}^{b_i} \boldsymbol{\Phi}_{ak}^T\boldsymbol{\Phi}_{\xi}dXd\boldsymbol{q} \tag{17}$$

collecting all the actuator equations, we obtain

$$d\boldsymbol{y} = \boldsymbol{B}(\boldsymbol{q})^T d\boldsymbol{q} \tag{18}$$

in matrix form [64].

Equation (16) is used to determine the variation in length of the threadlike actuators, $\boldsymbol{y_a}$, as a function of the soft robot's deformation. It can also be used to compute the length variation of the strain sensors, $\boldsymbol{y_s}$. The only difference lies in the integration interval, which is adjusted to account for the specific regions where the sensors or actuators are located, as well as the specific path of the threadlike elements inside the soft body.

B. Forward Solutions

The complete kinetostatic model of the continuum robot is described by (10) and (16). By inputting actuation $\boldsymbol{y}_a$ and external forces, $\boldsymbol{\mathcal{F}}_k$, the forward solution of the strain model can be estimated, including the entire shape, $\boldsymbol{q}$, and the actuation loads $\boldsymbol{u}$. The algebraic system of $n + n_a$ nonlinear equations and $n + n_a$ unknowns can be solved using a root finding algorithm for these inputs and outputs. We implement the trust-region-dogleg algorithm through the MATLAB function *fsolve* to solve the system. Once the shape of the robot is computed, the estimated length change of the stretch sensors can be obtained using (16), based on the position of each sensor segment.

C. Local Strain-Based Force and Shape Sensing

We formulate the problem of estimating the shape and external forces acting on sensorized, threadlike actuator-driven continuum robots using actuator displacements $\boldsymbol{y_a}$ and the measurement of the sensors $\boldsymbol{y_s}$. We introduce a new vector combining these lengths, defined as $\boldsymbol{Y} = [\boldsymbol{y_a}^T\ \boldsymbol{y_s}^T]^T$. The proposed method estimates the generalized coordinates $\boldsymbol{q}^\mathfrak{e}$, which define the manipulator's shape, and the external forces $\boldsymbol{F}_k^\mathfrak{e}$, ensuring that the actuator and sensors lengths $\boldsymbol{Y}^\mathfrak{e}(\boldsymbol{q}^\mathfrak{e})$ match the measured values $\boldsymbol{Y^m}$ while satisfying the static equilibrium model. Based on the estimated generalized coordinates $\boldsymbol{q}^\mathfrak{e}$, the length measurement error can be defined as

$$\boldsymbol{E}(\boldsymbol{q}^\mathfrak{e}) = \boldsymbol{Y}^\mathfrak{e}(\boldsymbol{q}^\mathfrak{e}) - \boldsymbol{Y^m}. \tag{19}$$

Then, we define the following minimization problem:

$$\begin{cases} \min_{\boldsymbol{q}^\mathfrak{e},\boldsymbol{\mathcal{F}}_k^\mathfrak{e},\boldsymbol{u}^\mathfrak{e}} & \|\boldsymbol{E}(\boldsymbol{q}^\mathfrak{e})\|_2^2 \\ \text{s.t.} & \boldsymbol{K}(\boldsymbol{q}^\mathfrak{e}) = \boldsymbol{B}(\boldsymbol{q}^\mathfrak{e})\boldsymbol{u^e} + \boldsymbol{Q}^\mathfrak{e}(\boldsymbol{q}^\mathfrak{e}). \end{cases} \tag{20}$$

In this minimization problem, the unknown variables are the generalized coordinates $\boldsymbol{q}^\mathfrak{e}$, the magnitudes of the external forces $\boldsymbol{\mathcal{F}}_k^\mathfrak{e}$ and the reaction forces in the rods $\boldsymbol{u^e}$. Although the reaction forces in the rod are not directly required in our problem, they must be estimated to compute the static equilibrium, which depends on these values.

Notice that by estimating $\boldsymbol{Q}^\mathfrak{e}$ under the assumption that we know the force locations, we can compute $\boldsymbol{J}_k^T \mathrm{Ad}^*_{\boldsymbol{g}_{\theta_k}^{-1}}$ based on $\boldsymbol{q}^\mathfrak{e}$, and we only have to estimate $\boldsymbol{\mathcal{F}}_k^\mathfrak{e}$. We assume in this work that the angular components of the wrenches are zero, so we only need to estimate the coordinates of $\boldsymbol{F}_k^\mathfrak{e}$.

D. Calculation of Sensitivity Ellipsoids

The model presented in this work is based on the static equilibrium of the robot system. From these equilibrium equations, we introduce a new concept, called sensitivity ellipsoids. This ellipsoid is a geometric representation that characterizes how sensitive the sensor measurements are to applied forces in different directions. It can be calculated at any position along the soft body, such as the sensitivity ellipsoids at the middle or tip of each module as shown in Fig. 1.

Similarly to the compliance ellipsoid presented in [54] and [61], which relates the linear displacement of the tip to an external force applied at any point on the robot, we derive a new ellipsoid that relates the change in sensor strain to a force applied at a specific point along the robot. To achieve this, we combine the kinematic formulation developed in [64], which relates the change in sensor strain to variations in the generalized coordinates, with the static equilibrium equations. We use a linearization of the pair $(\boldsymbol{q}, \boldsymbol{\mathcal{F}}_k)$ in the static equilibrium (10). Assuming that $\delta \boldsymbol{J}_k^T/\delta \boldsymbol{q} \approx 0$, we obtain the same relation typically used for the compliance ellipsoid:

$$\boldsymbol{K}\delta\boldsymbol{q} = \boldsymbol{J}_k^T \delta\boldsymbol{\mathcal{F}}_k^b \tag{21}$$

where $\boldsymbol{\mathcal{F}}_k^b$ is the wrench expressed in the body-frame coordinates, given by $\boldsymbol{\mathcal{F}}_k^b = \mathrm{Ad}^*_{\boldsymbol{g}_{\theta_k}^{-1}}\boldsymbol{\mathcal{F}}_k$. Considering an infinitesimal change in the strain sensor given by $\delta\boldsymbol{y_s} = \boldsymbol{B}(\boldsymbol{q})^T\delta\boldsymbol{q}$ from (18), and the Jacobian $\boldsymbol{J}_k = [\boldsymbol{J}_1^T\ \boldsymbol{J}_2^T]^T$, which includes both linear and angular components evaluated at the point of force application, we can, using (21), allows us to derive the following new 3-D linear ellipsoid:

$$\delta\boldsymbol{y_s} = \boldsymbol{B}(\boldsymbol{q})^T\boldsymbol{K}^{-1}\boldsymbol{J}_2^T\delta\boldsymbol{F}_k^b = \hat{\boldsymbol{J}}\delta\boldsymbol{F}_k^b \tag{22}$$

where $\hat{\boldsymbol{J}} \in \mathbb{R}^{n_s\times 3}$ and n_s is the number of sensors. The sensitivity ellipsoid is then defined as $\boldsymbol{M} = (\hat{\boldsymbol{J}}^T\hat{\boldsymbol{J}})^{-1}$. The eigenvalues $\lambda_i(\boldsymbol{M})$ correspond to the squared lengths of the ellipsoid's principal axes $\boldsymbol{\nu}_i(\boldsymbol{M})$. Each eigenvalue represents the extent to which the sensor lengths change in the direction of the corresponding eigenvector for a unit force applied. A larger eigenvalue indicates that a unit force input produces a greater change in sensor length. We propose using the visualized ellipsoid to assess the sensitivity of the sensors in estimating external forces applied to soft robots—particularly forces acting along the backbone, which induce very small deformations and are thus more challenging to estimate.

V. Robotic Prototype and System

A. Rod-Driven Soft Continuum Robot

In this article, a specific RDSR with embedded stretch sensors is used for simulation and experimental investigation. This robot has two-module soft bodies with eGaIn-based piecewise soft sensor (PSS) embedded on the surface of the silicone as shown in Fig. 3(a). The structure and principle of the actuation, data collection, and control module are explained in detail in related work [5], [11]. A brief introduction of this robot system is described as follows.

Each module consists of a cylindrical hollow silicone-based body, end and base disk with internal lock rings, three flexible rods (NiTi rods) and silicone tubes [see Fig. 3(b)]. One side of

TABLE I
SHAPE AND MATERIAL PARAMETERS OF RDSR

NiTi Rod	Young's Modulus (GPa)	10
	Radius (mm)	0.65
	Position radius (mm)	16
Silicone body	Young's Modulus (KPa)	110
	Initial length (mm)	160
	Inner radius (mm)	12.5
	Outer radius (mm)	21
Fiber position radius (mm)		18
Sensors position radius (mm)		21
Length of connector (mm)		18

each rod passes through the silicone tube and is fixed to the end disk by lock rings. The other side is fixed to the slider in the actuation module. Then, the motor's rotational motion is converted into linear motion through the lead screw and slider to achieve push and pull actuation. The hollow silicone body, fabricated between the base and end disk, is reinforced by a fiber structure that can prevent large radial deformation and increase the bending capability when pushing and pulling the actuation rods. Each module RDSR realizes contraction, elongation, and bidirectional bending movement through push–pull coordinated control of three flexible rods.

Each PSS, consisting of three inner channels and separate strain sensors (first, second, third piece) [see Fig. 3(c)], is evenly embedded on the soft body along the circumferential direction. All PSSes are colocated as close as possible to the corresponding actuation rods so as to accurately capture the local strain in real time. The designed length and width of each PSS is 130 and 35 mm, respectively. Each piece has the same length, about 42 mm. When the silicone substrate is linearly stretched at both ends, the strain of each piece is the same. After assembly with the soft body, the actual length of each piece will vary due to inevitable fabrication errors. Strain sensors calibration is reported in Section VII-B.

Multimodule RDSRs [see Fig. 3(a)] are assembled in series via the 3-D-printed connector, and its exploded view is shown in Fig. 3(a)ii. The actuation rods of module 2 passes through the soft body of module 1, and all rods are placed evenly and circumferentially inside the silicone. The detailed relative position of rod 1, 2, 3 in module 1 and rod 4, 5, 6 in module 2 is shown in Fig. 3(a)i.

B. Identification of the Stiffness Matrix

The robot features a hybrid silicone–NiTi structure with a symmetric rod arrangement, ensuring the center of equivalent elasticity coincides with the geometrical center. The additional stiffness from the NiTi rods is computed using the previously validated equivalent elasticity matrix [19], where a constant Legendre polynomial basis was used for elongation, and a third-order Legendre polynomial basis was used for the two bending directions (y and z) for each soft link, resulting in a total of 18 DOFs. The model, tested on a one-module RDSR with three internal rods, accurately predicts the robot's shape under varying tip forces and rod lengths, achieving a maximum error of 6.1 mm (around 4 % of total length). The identified material

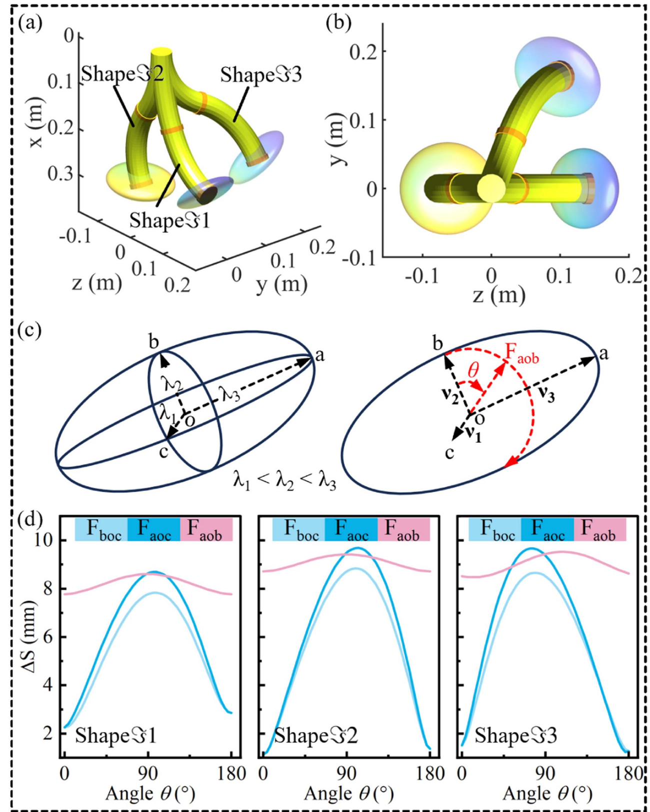

Fig. 4. Simulated results and sensitivity ellipsoids of shape $\Im$1, $\Im$2, and $\Im$3: (a) whole and (b) top view. (c) Schematic diagram of ellipsoid and the applied external tip force. (d) Total surface strain change $\triangle$S with different tip force applied in these three shapes. Scale of visualized ellipsoids: 0.01.

parameters of RDSR are shown in Table I. Rigid segments are modeled as pure translations between their endpoints.

VI. SIMULATIONS AND SENSITIVITY ANALYSIS

In this section, we assess our estimation approach and the validity of the visualized ellipsoid in identifying robot configurations where force estimation is feasible or not in real experiments. We test our algorithms in simulation on the continuum robot described in Section V.

A. Strain-Based Sensitivity

Three different shapes, $\Im$1, $\Im$2, and $\Im$3, are simulated under different external forces applied to the tip. The given rod lengths of these configurations are randomly chosen, but to ensure that $\Im$1 and $\Im$2 represents the typical in-plane bending shapes, "S" and "C" shapes, while shape $\Im$3 shows the out-plane bending shape. Fig. 4(a) and (b) shows these simulated shapes and sensitivity ellipsoids at the tip position. The rod lengths, eigenvalues, and eigenvectors are listed in Table II. It should be noted that a large difference between the eigenvalues will result in a flatter ellipsoid. To make it more intuitive, when representing the ellipsoids in the figures, the principal axes $\boldsymbol{\nu}_1$, $\boldsymbol{\nu}_2$, and $\boldsymbol{\nu}_3$ of the visualized ellipsoid are equally scaled.

Initially, eigenvectors $\boldsymbol{\nu}_1$, $\boldsymbol{\nu}_2$, and $\boldsymbol{\nu}_3$ and eigenvalues λ_1, λ_2, and λ_3 of the ellipsoid are obtained as listed in Table II. Then, the

TABLE II
EIGENVECTORS AND EIGENVALUES OF SHAPE $\Im 1$, $\Im 2$, AND $\Im 3$ WITHOUT APPLIED EXTERNAL LOADS

Configurations (m)			$[\boldsymbol{\nu}_1; \boldsymbol{\nu}_2; \boldsymbol{\nu}_3]$			$[\lambda_1; \lambda_2; \lambda_3]$
Rod lengths of $\Im 1$			0.7729	0	0.6345	2.0373
0.15	0.16	0.16	0	1	0	5.8767
0.29	0.32	0.29	0.6345	0	-0.7729	6.4469
Rod lengths of $\Im 2$			0.9907	0	0.1361	2.0348
0.15	0.145	0.145	0	1	0	6.7331
0.31	0.32	0.31	-0.1361	0	0.9907	7.0332
Rod lengths of $\Im 3$			-0.7524	0.0110	-0.6587	1.9179
0.145	0.17	0.14	-0.5311	-0.6018	0.5965	6.6555
0.315	0.325	0.31	-0.3898	0.7986	0.4586	7.0181

changes of entire shape and local sensor strains under different tip external forces were simulated. As shown in Fig. 4(c), assuming $\lambda_1 < \lambda_2 < \lambda_3$, the applied force satisfies the following two conditions: first, the direction changes from the eigenvector with a smaller eigenvalue to the eigenvector with a larger eigenvalue, and second, the magnitude of the given force is a constant, which is 5N. For example, the force F_{aob} is located in plane aob, and its direction θ changes from $\boldsymbol{\nu}_2$ to $\boldsymbol{\nu}_3$, so the force rotates around $\boldsymbol{\nu}_1$.

The strain sensitivity $\triangle$S is defined in this work as the total changes of local strains when an external force is applied to the system, which can be calculated based on sensor strains before and after applying external forces as follows:

$$\Delta \mathrm{S} = \sqrt{\sum_{i=1}^{18} \left(\mathrm{S}_i|_F - \mathrm{S}_i|_0\right)^2} \tag{23}$$

where S_i denotes the sensor strain in 18 pieces of the whole robot, which is in order from the first to third piece of rod 1–6 as shown in Fig. 3(a). $|_F$ and $|_0$ indicate whether the external force is applied or not, respectively. $\triangle$S reflects the sensitivity of the local strain to external forces under a specific configuration. In this article, we use strain sensitivity to quantitatively validate the functionality and capabilities of the visualization ellipsoid.

The simulation results [see Fig. 4(d)] indicate that these typical configurations (Shapes $\Im 1$, $\Im 2$, and $\Im 3$) retain the same variation characteristics in strain sensitivity $\triangle$S. The closer the external force is to the eigenvector with a larger principal length, the higher the strain sensitivity of the robot arm. All cases under applied force F_{aob} has much larger and almost unchanged sensitivity due to λ_2 and λ_3 are almost the same and much larger than λ_1 (as shown in Table II). The sensitivity increases to 9 mm around the angle of 90°when the direction of applied force F_{boc} or F_{aoc} ranges from $\boldsymbol{\nu}_1$ to $\boldsymbol{\nu}_2$ or $\boldsymbol{\nu}_1$ to $\boldsymbol{\nu}_3$. These results validate the importance of the proposed visualized ellipsoid in identifying configurations where external forces are easier to estimate, as they have a greater influence on strain variation. Therefore, the robot configuration can be adjusted so that the eigenvector with a larger length closer to the direction of the force, making the local strain sensors more sensitive to external stimuli and enabling the strain-based estimator to better observe the external forces.

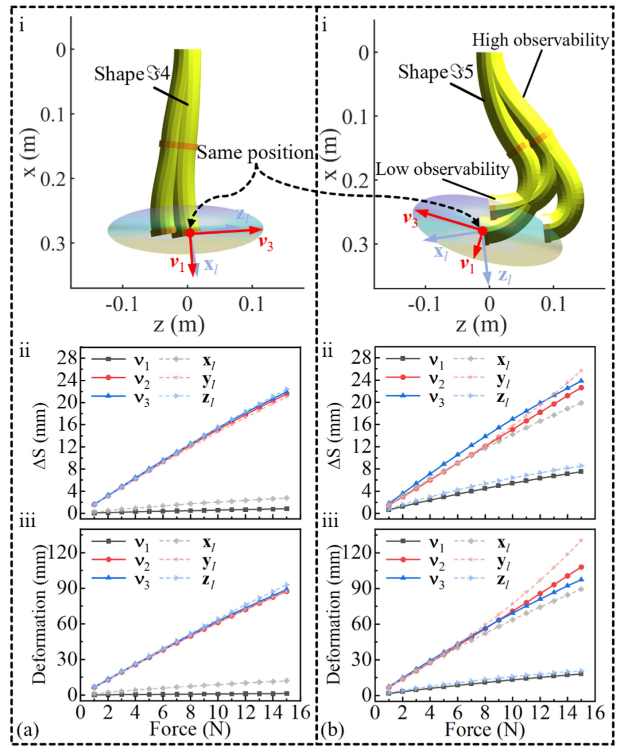

Fig. 5. Sensitivity analysis of sensor strain under varied forces along eigenvectors ($\boldsymbol{\nu}_1$, $\boldsymbol{\nu}_2$, $\boldsymbol{\nu}_3$) and local frame axis (x_l, y_l, z_l). Deformed shapes with low ($\boldsymbol{\nu}_1$) and high ($\boldsymbol{\nu}_3$) sensitivity for (a)(i) shape $\Im 4$ and (b)(i) $\Im 5$. (a)–(b)(ii) Comparison of the sensitivity $\triangle$S and (iii) deformed tip distance with respect to different tip forces. Scale of visualized ellipsoids: 0.02.

B. Sensitivity Analysis Under Different Magnitude Forces

The strain sensitivity $\triangle$S is also analyzed under varied forces from 0 to 15 N with intervals of 1 N along directions of eigenvectors ($\boldsymbol{\nu}_1$, $\boldsymbol{\nu}_2$, $\boldsymbol{\nu}_3$) and local frame axis (x_l, y_l, z_l). Two different shapes ($\Im 4$ and $\Im 5$) with the same tip position are obtained by giving different rod lengths, [0.146; 0.144; 0.144; 0.269; 0.273; 0.269] m and [0.145; 0.16; 0.16; 0.33; 0.295; 0.33] m, respectively [shown in Fig. 5(a)–(b)i]. The sensitivity $\triangle$S and tip deformation varied with forces are shown in Fig. 5(a) and (b)ii and iii. The tangential direction (local x-axis) of shape $\Im 4$ is almost aligned with the eigenvector $\boldsymbol{\nu}_1$ with the smallest eigenvalue λ_1, but for shape $\Im 5$, the tangential direction is almost aligned with the eigenvector $\boldsymbol{\nu}_3$ with the largest eigenvalue λ_3.

As results demonstrate, the sensitivity and deformation of $\Im 4$ and $\Im 5$ under forces along $\boldsymbol{\nu}_1$ are much smaller than those under forces along $\boldsymbol{\nu}_3$, which is consistent with the result obtained from Section VI-A. Meanwhile, the sensitivity and deformation of $\Im 4$ under forces along x_l are smaller than those under forces along z_l. This means that external forces along x_l (tangential direction) produce lower sensor strain sensitivity, which is one of the motivations for assuming that the applied forces are orthogonal to the robot backbone. However, the opposite result occurs in $\Im 5$. The robot arm achieves much higher strain sensitivity in external forces applied along x_l. Although the external force along z_l is perpendicular to the robot backbone in this shape, higher strain sensitivity can be obtained by applying the force along the x_l aligned with the robot backbone. Due to the near-ill-conditioned situation in the tangential direction of the backbone in shape $\Im_4$, it is practically impossible to sense the external force with acceptable error in the presence of noise and measurement errors in the strain sensors, as will be demonstrated later. The visualized ellipsoid can be used to determine if the local strain is sensitive to force. Some configurations should be adjusted to avoid local strains being insensitive to external forces.

C. *Effect of Strain Errors on Different Configurations With Varying Sensitivity*

Achieving perfect alignment between model-predicted local strains and sensor measurements is inherently challenging. In practice, errors in strain measurements from real sensors affect force estimation differently depending on the sensitivity $\triangle$S of a specific configuration. To quantify the impact of such strain errors on force estimation, we characterize the performance of our force estimator by deliberately introducing controlled strain errors into the model for each soft sensor. In our simulation, we simultaneously consider shapes $\Im 4$ and $\Im 5$ (as described in Section VI-B), which exhibit significantly different sensitivity characteristics, thereby allowing us to examine the influence of sensor errors under diverse conditions.

Fig. 6(a) illustrates the overall simulation process. In the simulation, a fixed external force $\mathrm{F_{set}} = 2$ N is applied along the x_l (tangential) and z_l (perpendicular) axes for shapes $\Im 4$ and $\Im$ 5, respectively. The strain model computes the initial guess, and then, predicts the sensor strain in the corresponding regions. Next, we introduce a random strain error uniformly sampled in the range [-ds, ds] into the force estimator. Finally, we use the solutions at a set force of 0 N as the initial guess to estimate the force $\mathrm{F_{est}}$ along the given directions.

We perform simulations with strain error magnitudes ds of 0.2, 0.6, and 1.0 mm for each soft sensor. Two primary findings emerge from the simulation results for shape $\Im 4$ [see Fig. 6(b)]. First, the force estimation error and its standard deviation σ along the tangential direction (x_l-axis) are significantly high, with σ reaching up to 2N, indicating a low sensitivity of the sensors in this direction. Second, when the force is applied perpendicular to the backbone (z_l-axis), the estimation is both more accurate and robust, with the maximum standard deviation σ being approximately 0.6 N. Conversely, in the simulation with Shape $\Im 5$ [see Fig. 6(c)], the simulation reveals that the maximum standard deviation σ of the estimated force is approximately 0.6 N along the tangential direction and 0.8 N in the perpendicular direction. Overall, $\Im 5$ exhibits better force estimation performance with reduced error and lower data fluctuations compared to $\Im$ 4. Notably, even when the strain error is as high as 1 mm, the standard deviation σ for force estimates in directions with high sensitivity does not exceed 0.6 N. Conversely, when the external forces along directions with low observability, the estimation becomes considerably more difficult.

VII. Experimental Validations

In this section, the proposed methodology is tested on the continuum robot described in Section V to demonstrate the effectiveness of our method with real prototypes.

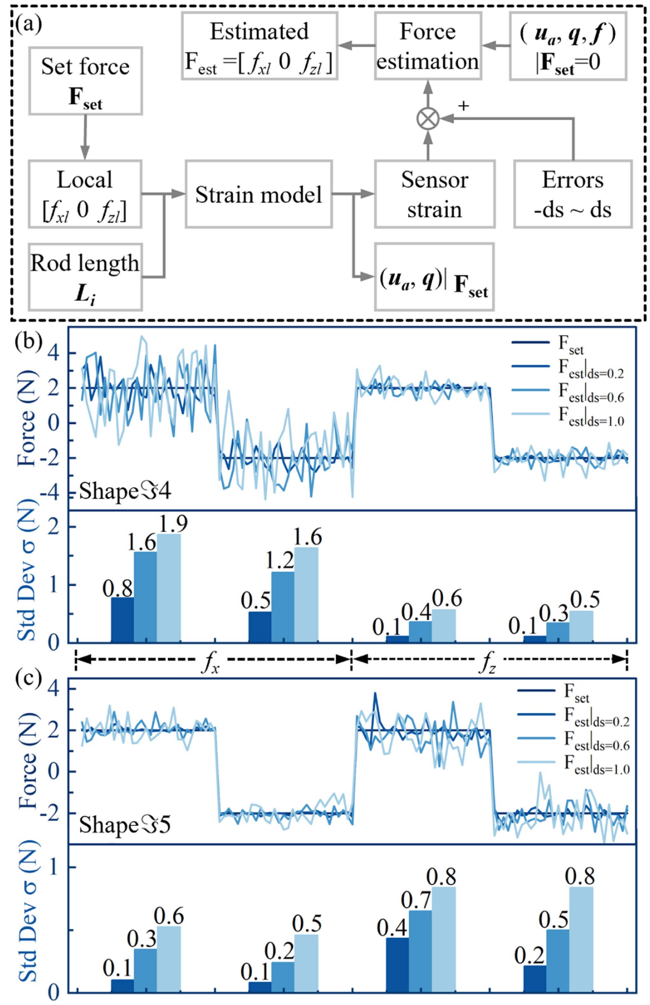

Fig. 6. Simulation results of force estimation and strain sensitivity analysis. (a) Simulation process of the effect of sensor error on force estimation. The estimated forces of (b) shape $\Im 4$ and (c) $\Im$ 5 under different sensor errors of 0.2, 0.6, 1.0 mm, respectively. Std. Dev. σ: Standard deviation.

A. *Tip Position Estimation*

Initially, we randomly generated 500 experimental configurations of RDSR. For each configuration, the RDSR was actuated under both unloaded conditions and with external loads of 100, 200, and 300 gram-force (gf). The tip position was recorded using a RealSense D435 RGB-D camera, which provided the ground truth, while sensor voltages were acquired via an NI USB-6218 data acquisition system.

For each configuration and load condition, our model predicts the shape of the robot, yielding estimated positions along its entire body. The estimation error e is computed as the Euclidean norm between the estimated tip position $\mathbf{p}_{\text{model}}$ and the ground-truth position $\mathbf{p}_{\text{actual}}$ as

$$e = ||\mathbf{p}_{\text{model}} - \mathbf{p}_{\text{actual}}||. \quad (24)$$

Fig. 7 presents the error metrics under the various loading conditions. On average, the error is less than 6 mm, which corresponds to under 1.8% of the 330-mm body length. The error distribution indicates that most errors are centered around 5 mm, with a range from 3 to 8 mm. Moreover, the reconstructed

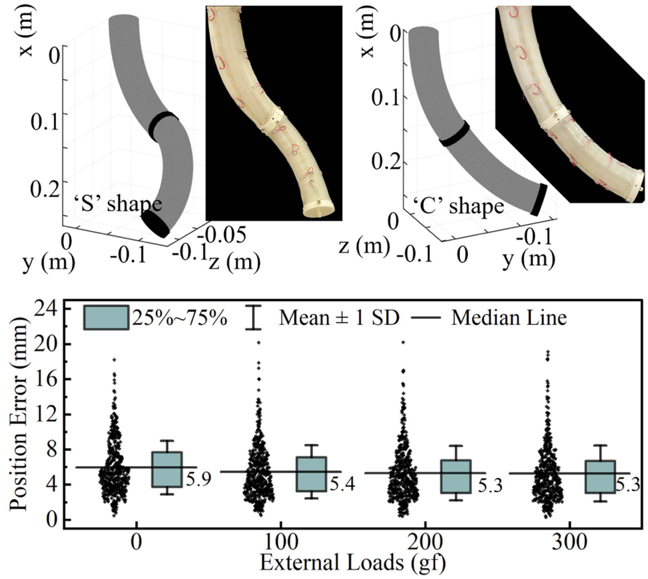

Fig. 7. Tip position error distribution and box plot of RDSR under different external loads (0, 100, 200, 300 gf). It includes simulations of different shape deformations such as multidirectional bending ("S" and "C" shapes).

TABLE III
CALIBRATION AND FITTING RESULTS OF EACH SOFT SENSOR

Strain = $a(\Delta R/R_0)^2 + b(\Delta R/R_0) + c$

	a	b	c	R^2		a	b	c	R^2
S_1	-11.09	3.6	-0.005	0.9976	S_{10}	-14.18	5.02	-0.004	0.9985
S_2	-7.89	2.91	-0.001	0.9997	S_{11}	55.24	1.42	-0.098	0.9750
S_3	-14.42	3.34	-0.004	0.9960	S_{12}	-9.43	4.18	-0.005	0.9980
S_4	-6.34	4.46	-0.001	0.9998	S_{13}	-9.77	3.16	-0.002	0.9995
S_5	-15.65	3.84	0.012	0.9999	S_{14}	-5.45	2.88	-0.006	0.9985
S_6	-20.79	4.08	0.001	0.9974	S_{15}	-8.28	4.22	-0.006	0.9993
S_7	-52.47	5.85	-0.007	0.9974	S_{16}	-10.91	3.49	-0.004	0.9991
S_8	-10.68	3.79	-0.003	0.9994	S_{17}	-2.34	3.20	-0.006	0.9998
S_9	-18.81	3.77	0.001	0.9968	S_{18}	-2.05	2.89	-0.006	1.0000

shapes closely match those obtained from the actual measurements, thereby avoiding redundant solutions for the tip position. These results demonstrate that the strain-based model accurately captures the deformation and predicts the shape of the RDSR under both actuation and external loadings.

B. Predicted Local Sensor Strain

We calibrated the sensory system by establishing a quantitative relationship between the sensor resistance and the corresponding strain for each soft sensor (see Table III). In our calibration procedure, the robot arm in module 1 was actuated through its entire range from shortest to longest state, while concurrently, the sensors in module 2 exhibited complementary changes (i.e., transitioning from their longest to shortest states). All actuation rods were simultaneously pulled or pushed to induce the extensible motion. At each actuation step, the actual sensor length was measured and the corresponding resistance was recorded, thereby providing the complete calibration dataset.

A quadratic polynomial was then fitted to the normalized resistance change versus sensor strain data. The fitted coefficients, as listed in Table III, demonstrate a goodness-of-fit close to 1.

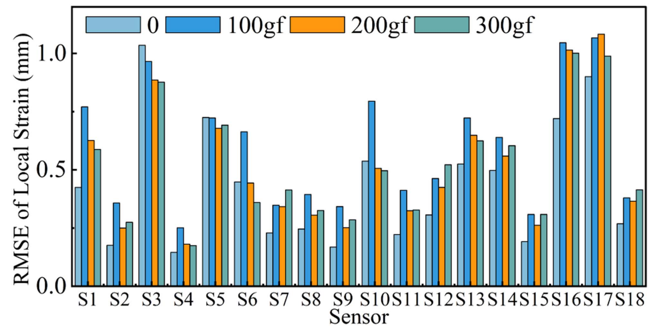

Fig. 8. RMSE of predicted sensor lengths under 0, 100, 200, 300 gf loads. RMSE: root-mean-square error.

Consequently, the resistance can be used to reliably compute the measured strain via the fitted relationship.

Once the forward solution for the robot shape is obtained, the local strain at each sensor can be predicted. In practice, the integration in (16) is performed only over the sensor's effective region. For example, for the sensor in module 1 that is aligned with rod 1, integration is performed only over the spatial interval corresponding to that sensor [e.g., from the starting position (3, 50, 107) mm to the ending position (47, 90, 140) mm].

Based on the model's predicted length change $\Delta l_{\text{prediction}}$, and the actual length change measured from sensory feedback Δl_{actual}, we compute the sensor estimation error as: $e_{\text{sensor}} = \Delta l_{\text{prediction}} - \Delta l_{\text{actual}}$. To quantify the overall accuracy of the predicted strain, we calculate the root-mean-square error (RMSE) as follows:

$$\delta_{\text{sensor}} = \sqrt{\frac{1}{n} \sum_{i=1}^{n} \left(\Delta l_{\text{prediction}} - \Delta l_{\text{actual}}\right)^2}. \quad (25)$$

All experimental configurations were tested under external loads of 100, 200, and 300 gf. Fig. 8 shows the RMSE of the length change under these load conditions. In most cases, the prediction errors are no more than 1 mm, with an average error of approximately 0.5 mm and the maximum RMSE as a percentage of the actual sensor length does not exceed 2%. These experimental results confirm that the strain model reliably predicts the sensor strain.

C. Estimation of Forces Orthogonal to the Backbone

The experiments were performed under two distinct configurations (shape $\Im 6$ and $\Im 7$) with rod lengths of [0.16, 0.16, 0.16, 0.32, 0.32, 0.32] m and [0.15, 0.163, 0.163, 0.319, 0.313, 0.319] m, respectively. In each configuration, static forces were applied to the soft body at two locations: at the tip and at the middle of the soft arm. For each location, forces were applied along various directions, specifically, in the yz-plane of the local coordinate frame, at angles from 0° to 315° in 45° increments (i.e., forces orthogonal to the backbone). Fig. 9(a)–(d)i schematically depicts these directions in the local frame.

In the actual experiment, we set a threshold (less than 0.1 N) for the tangential force (local x-axis) to ensure that the applied force is in the yz-plane. The force magnitudes applied at the middle of the arm differed from those at the tip in order to

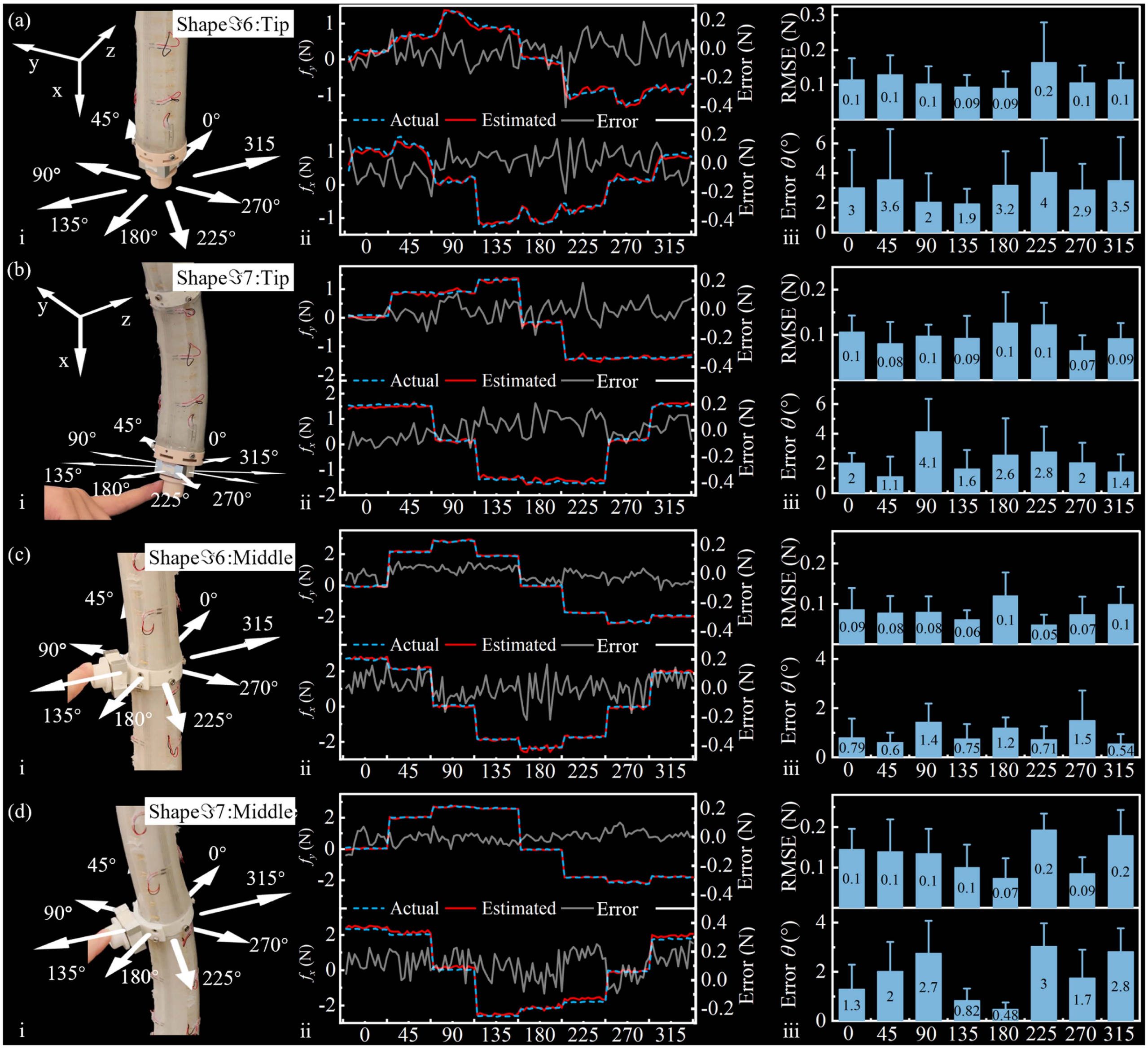

Fig. 9. Estimation of forces (f_y, f_z) orthogonal to the backbone (local x-axis). Applying varied directional forces at two different position on two distinct configurations (shapes $\Im 6$ and $\Im 7$): (a)–(b)(i) tip and (c)–(d)(i) middle. (a)–(d)(ii) Actual and estimated force were recorded. Estimation errors of each axial force (local f_y and f_z) were qualified to evaluate the performance of the force estimation. (a)–(d)(iii) RMSE of the estimated force and the angular error.

TABLE IV
DIFFERENT EIGENVALUES AND SENSITIVITY OF THE TANGENTIAL FORCE ESTIMATION UNDER DIFFERENT CONFIGURATIONS

Configurations			$[\boldsymbol{\nu}_1;\ \boldsymbol{\nu}_2;\ \boldsymbol{\nu}_3]$			$[\lambda_1;\ \lambda_2;\ \lambda_3]$	Configurations			$[\boldsymbol{\nu}_1;\ \boldsymbol{\nu}_2;\ \boldsymbol{\nu}_3]$			$[\lambda_1;\ \lambda_2;\ \lambda_3]$
λ_{xl} = 1.90			0.9614	0.2750	0	1.9021	λ_{xl} = 2.56			0.9889	0	0.1488	2.0666
0.16	0.165	0.156	0.2750	-0.9614	0	6.5896	0.16	0.17	0.15	0.1488	0	-0.9889	6.5083
0.303	0.30	0.296	0	0	1	6.6393	0.307	0.314	0.321	0	1	0	6.6171
λ_{xl} = 1.97			0.9724	0.2332	0	1.9150	λ_{xl} = 3.25			0.9949	0	0.1008	2.2169
0.16	0.166	0.154	0.2332	-0.9724	0	6.5828	0.16	0.172	0.149	0.1008	0	-0.9949	6.3972
0.301	0.301	0.301	0	-0.0344	0	6.6253	0.316	0.327	0.338	0	1	0	6.6574
λ_{xl} = 2.17			0.9813	0	0.1924	1.9685	λ_{xl} = 3.61			0.9967	0	0.0816	2.2857
0.16	0.168	0.152	0.1924	0	-0.9813	6.5835	0.163	0.175	0.151	0.0816	0	-0.9967	6.3011
0.302	0.306	0.309	0	1	0	6.5932	0.32	0.334	0.345	0	1	0	6.6244

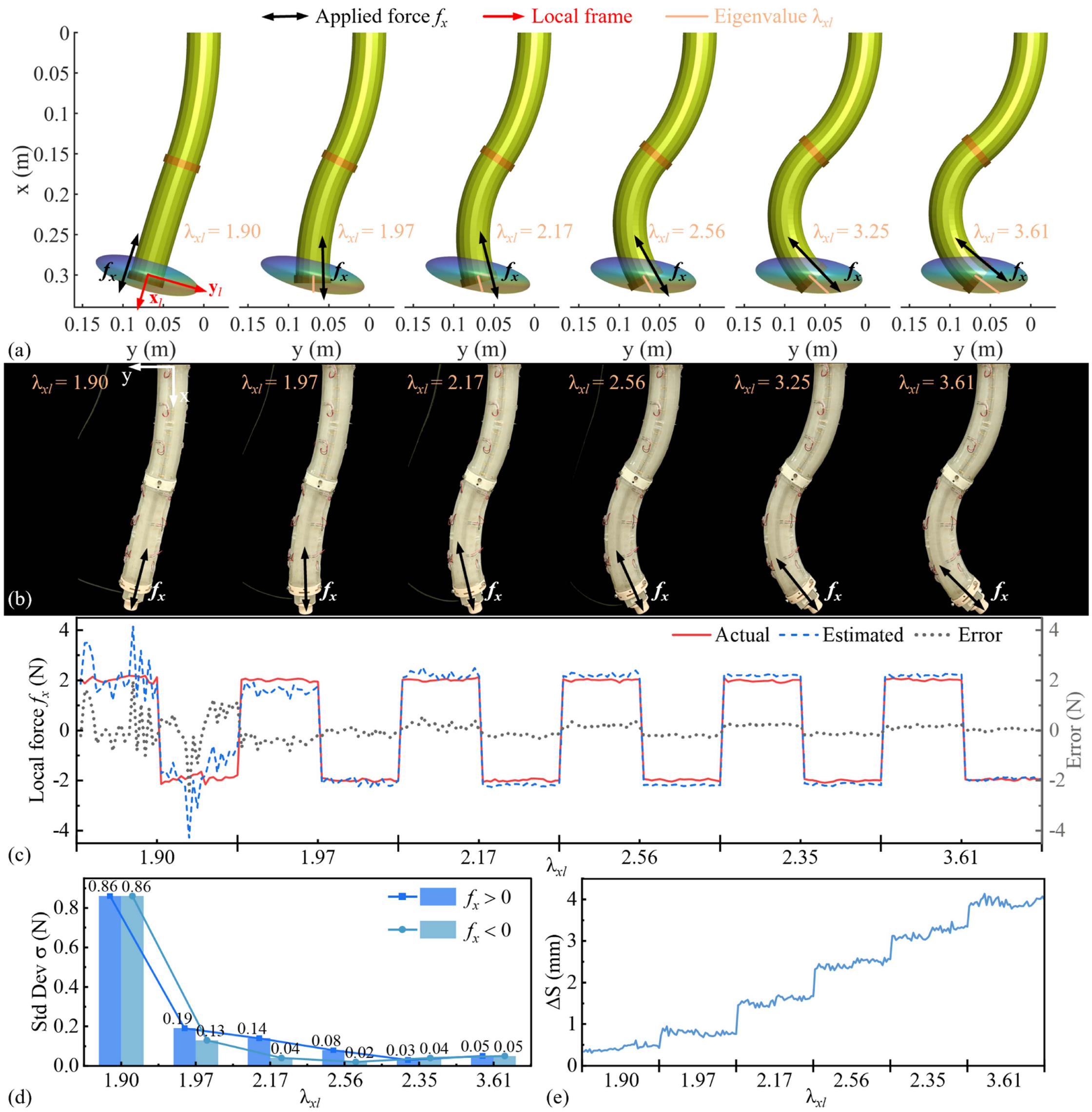

Fig. 10. Validation of tangential force estimation considering sensitivity $\triangle$S. (a) Simulated configurations at the tip with different sensitivity (eigenvalue λ_{xl}: 1.90, 1.97, 2.17, 2.56, 3.25, 3.61). (b) Experimental configurations in real conditions. (c) Actual and estimated force tangential to the backbone (local force f_x) and their errors. (d) Standard deviation σ of the estimation error. (e) Variation of strain sensitivity $\triangle$S with different configurations. Scale of visualized ellipsoids: 0.01.

validate the strain-based estimation across varying load distributions. For each directional case (0° to 315°), at least ten force measurements were collected. Both the actual force [measured by a three-axis force sensor with an accuracy of 0.3% of the range (0–20 N)] and the corresponding sensor resistance were simultaneously recorded. The estimated force was then computed from the actual sensor strain using the strain-based sensing method described in Section IV-C.

Fig. 9(a)–(d)ii shows the errors between the actual and estimated forces for the eight directional cases for each configuration. The estimated force profiles closely match the actual measurements, with most errors falling within the range of -0.4–0.4 N. To further quantify the estimation performance of the forces perpendicular to the backbone, the RMSE of the resultant force composed of f_y and f_z, as well as the angular error between the estimated and actual force vectors, were calculated. For forces applied at the middle of the arm, both the RMSE and angular error exhibited minimal fluctuations [see Fig. 9(a) and (c)iii], indicating robust and stable sensor performance. Fig. 9(b) and (d)iii exhibits higher error magnitudes at certain directional force, particular around 225° to 315°. The maximum RMSE of resultant forces is no more than 0.2 N and most angular errors remaining below 4.1°. Overall, the proposed force estimator successfully evaluates external forces orthogonal to the backbone, with an average RMSE of 0.12 N and its percentage 5.08% relative to the measured forces.

D. Tangential Backbone Force Estimation With Different Sensitivity

In our strain-based estimator, tangential backbone force along the robot's backbone can be observed from local strain

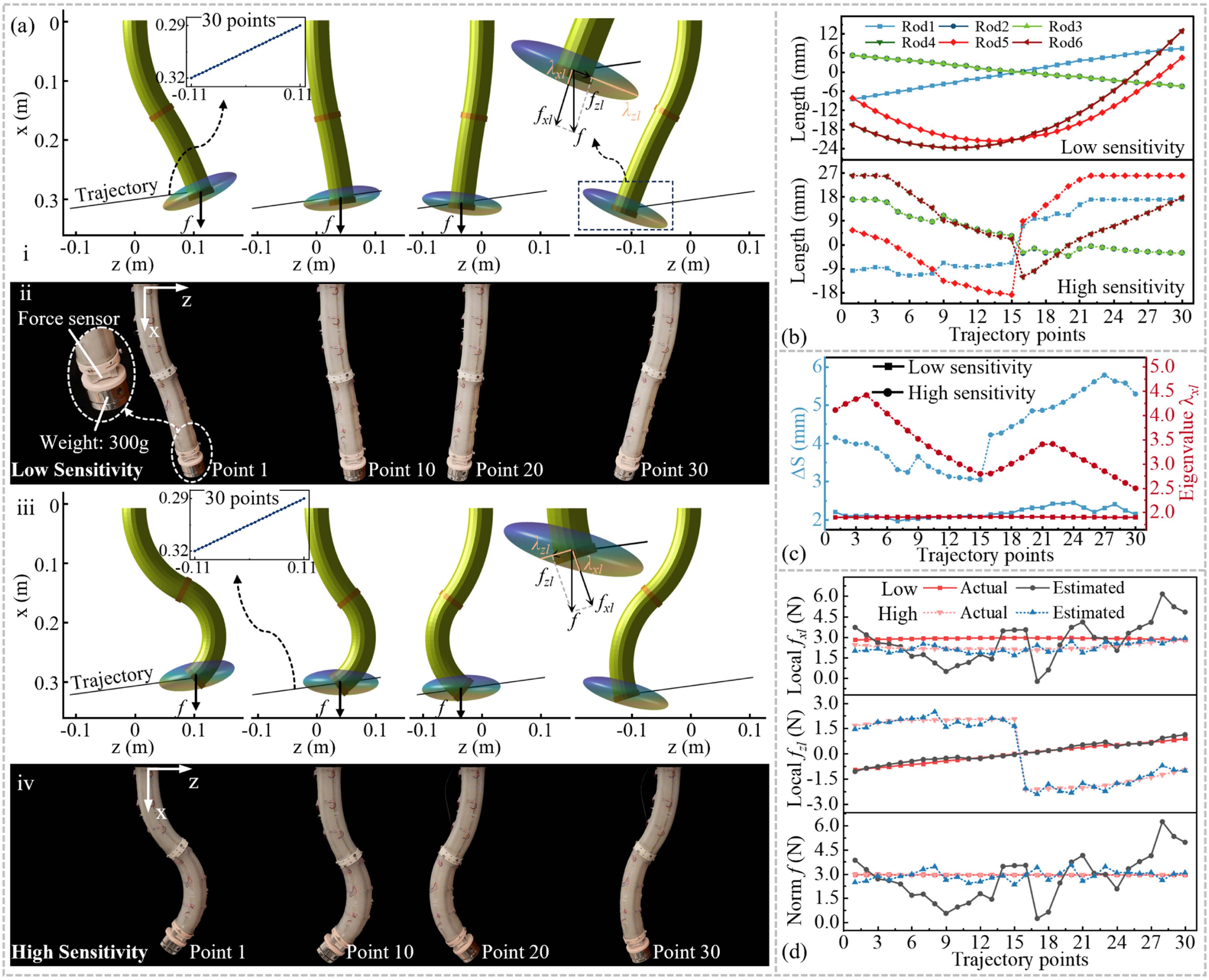

Fig. 11. Estimation of vertical forces in trajectory tracking under low and high sensitivity. (a)(i) and (ii) Two distinct actuation strategies are generated and (ii) and (iv) applied in the actual soft arm. (b) Variation of rod length at each trajectory point. (c) Strain sensitivity $\triangle$S and eigenvalues λ_{xl} along the direction of applied weight. (d) Estimated accuracy of the local x-axis (f_{xl}), local y-axis (f_{yl}) and the resultant force (norm f). Scale of visualized ellipsoids: 0.01.

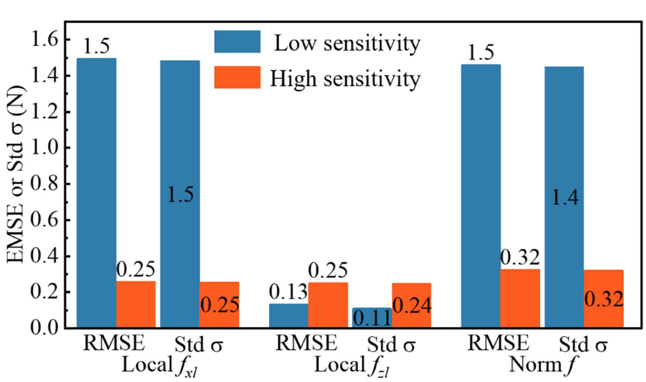

Fig. 12. Evaluation (RMSE and standard deviation σ) of vertical force estimation in trajectory tracking.

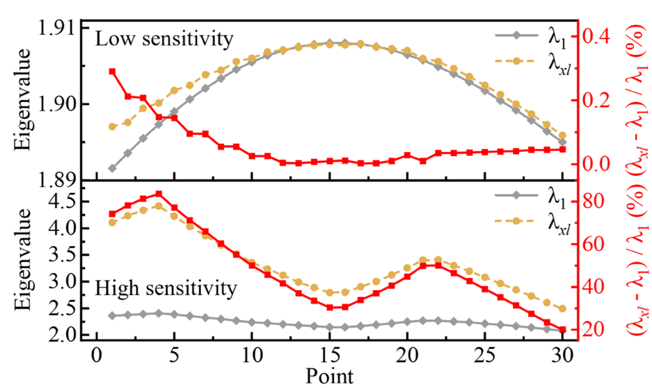

Fig. 13. Percentage of the tangential eigenvalue λ_{xl} relative to the minimum eigenvalue λ_1 in trajectory tracking.

measurements. However, since the strain sensitivity $\triangle$S of a directional force varies with the robot configuration, it is essential to consider this factor when applying the proposed method. To investigate the feasibility of tangential force estimation under varying sensitivity conditions, we conducted experiments on different configurations.

In this experiment, we generate multiple configurations by varying the rod lengths, which produced different visualized ellipsoids and corresponding strain sensitivity (see Table IV). Specifically, each configuration was tuned to increase the axial length of the ellipsoid along the tangential direction (local x-axis), as illustrated in Fig. 10(a). As the orientation and deformation of the soft arm increased, the eigenvalue λ_{xl} rose from 1.90 to 3.61. The percentage changes of λ_{xl} relative to λ_1 are 0%, 2.57%, 10.04%, 24.09%, 46.59%, and 57.92%, respectively. The percentage change is calculate as $|\lambda_{xl} - \lambda_1|/\lambda_1(\%)$. Subsequently, as shown in Fig. 10(b), we sequentially input the rod lengths into the robotic system controller, apply a tangential force f_{x} (around 2 N) at the tip, record the actual force, and compute the estimated force from the local sensor strain.

Fig. 10(c) compares the actual and estimated forces, with the estimation error plotted as a dotted line. For configuration with low sensitivity, such as $\lambda_{xl} = 1.90$, the estimator demonstrates the lowest fidelity, with major discrepancies attributable to insensitive strain changes due to external forces. As λ_{xl} increases, the strain sensitivity $\triangle$S increases from 0.5 to 4 mm [see Fig. 10(e)], the estimated force converges toward the actual measurement, and the maximum estimation error decreases from 2.41 to 0.24 N [see Fig. 10(c)]. The high sensitivity in the target direction increases the local strain observation of external forces and greatly improves the estimation accuracy of the tangential force. This demonstrates that the proposed visualized ellipsoids can be used to assess whether the tangential force can be reliably estimated in a given configuration.

Furthermore, we quantitatively analyze the standard deviation of the estimator under both positive and negative forces as shown in Fig. 10(d). The standard deviation σ is highest when the eigenvalue λ_{xl} is lowest, which corresponds to minimal strain sensitivity in tangential forces. As λ_{xl} increases to 3.61, the standard deviation σ decreases significantly, indicating improved sensitivity and accuracy in capturing the external force. Therefore, in the proposed estimator, the feedback error of the actual strain sensor has little effect on the evaluation of the tangential force with high sensitivity. Moreover, once the sensitivity reaches a high level and the strain sensor performance plateaus with further increases in curvature, both the estimation accuracy and the standard deviation stabilize. Overall, these results demonstrate that incorporating the visualized ellipsoid and sensitivity into the strain-based estimator can significantly enhance the tangential force estimation along the backbone.

E. Force Estimation in Trajectory Tracking

The objective of this experiment is to evaluate the performance of force estimation under varying strain sensitivity conditions while tracking a predefined trajectory [see Fig. 11(a)]. During the motion, a vertical weight of 300 gf is applied at the tip of the arm to generate a constant force magnitude and direction.

The linear trajectory is defined in the xz plane, with the x-coordinate ranging from 0.19 to 0.32 m and the z-coordinate ranging from 0.11 to -0.11 m. Two sets of configurations are generated, each corresponding to a different rod actuation, while ensuring that both sets track the same trajectory divided into 30 points. In one set, the actuation produces smooth motions in the control space [see Fig. 11(a)i and ii and (b)]. However, these configurations exhibit low strain sensitivity, with $\triangle\mathrm{S} < 2.5$ mm and small eigenvalues along the tangential direction ($\lambda_x < 1.9$) [see Fig. 11(c)]. The entire shape and corresponding visualized ellipsoid for several points (points 1, 10, 20, 30) are depicted in Fig. 11(a)i. The strain sensitivity for the tangential force is much lower than that of other directional forces. In contrast, a second group of configurations was generated by adjusting the rod actuation [see Fig. 11(a)iii and iv]. Although the sequential actuation from points 1 to 30 is not as smooth as the first group, especially the sudden change from points 15 to 16 [see Fig. 11(b)], they have larger eigenvalues λ_{xl} ranging from 2.5 to 4.5 and higher strain sensitivity $\triangle$S ranging from 3 to 6 mm [see Fig. 11(c)]. Consequently, the sensitivity of these configurations in vertical forces greatly increases compared to the smooth-actuation configurations [see Fig. 11(a)i and iii]. Moreover, the actual robot shapes at trajectory points 1, 10, 20, and 30 closely match the shapes simulated using our strain model for both groups of configurations.

Experimental results demonstrate the importance of strain sensitivity and ellipsoid for achieving accurate and robust force estimation, especially forces tangential to the backbone in soft continuum robotic system [see Fig. 11(d)]. In the case of low sensitivity, strain sensors are insufficient to robustly and accurately capture the local deformation of the soft body, resulting in increased error (RMSE = 1.5 N) and inconsistencies (Standard deviation $\sigma = 1.5$ N) in force estimation as shown in Fig. 12. In contrast, high sensitivity significantly improves the performance of force estimation (RMSE = 0.32 N, Standard deviation $\sigma =$ 0.32 N). For different configurations tracking the same trajectory, with the same load and significantly different sensitivity $\triangle$S, the largest difference in the estimates lies in the tangential force (local force f_{xl}), as shown in Figs. 11(d) and 12. The percentage changes of λ_{xl} relative to λ_1 are below 0.3% in low sensitivity and range from 20% to 80% in high sensitivity (see Fig. 13). The estimates in the orthogonal force (local force f_{zl}) present similar accuracy and robustness.

VIII. Conclusion

In this work, we proposed a strain-based 3-D force and shape evaluation model for RDSRs with embedded stretch sensors, which includes local deformation, actuation, and external interactions. We then constructed a specific RDSR architecture with eGaIn-based piecewise strain sensors to demonstrate the feasibility and principle of estimating full shape and 3-D forces using this approach and sensitivity ellipsoid. Experiments demonstrated that the strain-based method allows us to estimate the shape of designed RDSR (tip position error less than 1.8 % of the body length), the local strain variations in relevant regions (deformation error within 0.5 mm on average), and the external forces orthogonal to the backbone (with average RMSE of 5.08% and angular error within 4°). Moreover, we introduced a new visualized ellipsoid based on the strain method. Several simulations quantify how the strain sensitivity varies with different configurations and external forces. The higher the sensitivity, the less effect the sensor strain error has on the force estimation (applicable to both tangential and orthogonal forces). With the help of the visualized ellipsoid, we successfully and accurately observed the tangential forces by changing the configuration to improve the strain sensitivity $\triangle$S. As $\triangle$S increases from 0.5 to 4 mm, the accuracy and robustness of the estimation results are significantly improved, with the error decreasing from 2.41 to 0.24 N and the standard deviation σ reducing from 0.86 to 0.05 N. When faced with tracking a trajectory under constant force (300-gf weight), the optimized configurations with higher sensitivity achieved higher estimation performance (RMSE and $\sigma = 0.32$ N) compared to those with lower sensitivity (RMSE and $\sigma = 1.5$ N), especially for external forces tangential to the backbone. To summarize, the visualized ellipsoid can be used to determine insensitive forces in certain configurations and convert them into sensitive. Applying force or adjusting the configuration so that the force direction deviates from the minimum eigenvector $\boldsymbol{\nu}_1$ can improve force sensing and increase strain sensitivity.

As for how to distinguish whether a directional forces is sensitive in a particular configuration, the visualized ellipsoid and its projected eigenvalues λ_{xl} along the tangential direction can be used to intuitively evaluate the sensitivity of local sensor strains to external forces. As verified and found in Sections VII-D and VII-E, the estimation of tangential forces f_{xl} is inaccuracy if the variation of the eigenvalue λ_{xl} along tangential direction is very small or even zero relative to the minimum eigenvalue λ_1. As the percentage variation of λ_{xl} increases from 0% to 2.57% and even 80%, the estimation of the tangential force f_{xl} becomes more accurate and robust. In this case, the local strain is sensitive to the tangential component and our force estimator can observe them correctly. However, a large increase in the tangential eigenvalue λ_{xl} will lead to larger deformation and orientation [see Fig. 10(a)]. Simply increasing deformation and orientation to increase strain sensitivity will lead to a significant decrease in the stiffness of the continuum robot. From an application standpoint, the strain-based method is particularly relevant to scenarios in which slender continuum robots operate in constrained or contact-rich environments and require both geometric awareness and interaction force perception. It will be preferable to align the stiffer direction of the robot to reduce deflections and finish real tasks such as minimally invasive surgeries [65] and assistive interaction with humans [66] using soft continuum robots. However, from the perspective of perception, tangential forces along the stiffest direction cause minimum deformation and local strain sensitivity, which are difficult to observe and sense as validated in Figs. 10 and 11. Due to the redundant configurations at the same tip position, the estimation of tangential forces can be robust and accurate as long as there are slight changes relative to the singularity configuration, such as reconfiguring the first configuration to the third one in Fig. 10. Therefore, our approach does not require reconfiguring the robot into a completely different shape and the distal pose. Future work will be to quantitatively balance and optimize the projected eigenvalues, shape deformation, and robot stiffness.

It should be emphasized that all numerical analyses in this article are conducted on a specific sensorized RDSR. The obtained performance and estimation accuracy are therefore specific to this architecture. Nevertheless, the proposed method and the concept of the sensitivity ellipsoid are not limited to this specific robot. They can be extended to other slender continuum robots equipped with strain sensors such as those proposed by Alatorre et al. [3], Orekhov et al. [22], Truby et al. [23], Yan et al. [67], Zhao et al. [68], and An et al. [69]. For these systems, since their local strain can be formulated under a similar continuum mechanics and sensed in a similar manner, the same principles of strain-based estimation and sensitivity visualization can be applied, requiring only minor modifications of the model and parameters to fit their specific architectures. Besides, several studies have demonstrated the feasibility of fabricating miniature stretch sensors directly on continuum robots with diameters around 10 mm (e.g., [3]), suggesting that the proposed method could be validated in even smaller, and potentially more medically relevant, robotic systems in the future.

Extending the strain-based method to the position estimation of point, multicontact and distributed forces will also be one of the future works. Due to the redundancy of strain sensors (S1–S18), more variable forces can be included in the shape and force sensing. We primarily demonstrate the concept and functionality of the visualized ellipsoid and strain sensitivity at the tip, but the presented results are applicable to all points along the entire shape of the soft continuum robot. We will further explore and propose continuous ellipsoid space and strain sensitivity profile for entire shape. This will provide a theoretical basis for the continuous and multipoint interaction between soft robotic arms and the environment. Finally, we will also investigate strain sensitivity transfer strategies where the desired sensitivity would be optimized as a function of the robot and soft sensor. When designing the soft arm, the proposed concept can be used in the initial stage to optimize the robot parameters and the placement of the soft sensors and achieve best performance in terms of force output, force estimation and controllable manipulability.

Acknowledgment

Views and opinions expressed are however those of the author(s) only and do not necessarily reflect those of the European Union or the European Research Council. Neither the European Union nor the granting authority can be held responsible for them. This work was also supported in part by the National Research Foundation, Prime Minister's Office, Singapore under its Campus for Research Excellence and Technological Enterprise programme. The Mens, Manus, and Machina is an interdisciplinary research group of the Singapore MIT Alliance for Research and Technology (SMART) Centre.

References

[1] C. Laschi, B. Mazzolai, and M. Cianchetti, "Soft robotics: Technologies and systems pushing the boundaries of robot abilities," *Sci. Robot.*, vol. 1, no. 1, 2016, Art. no. eaah3690.

[2] M. Russo et al., "Continuum robots: An overview," *Adv. Intell. Syst.*, vol. 5, no. 5, 2023, Art. no. 2200367.

[3] D. Alatorre, D. Axinte, and A. Rabani, "Continuum robot proprioception: The ionic liquid approach," *IEEE Trans. Robot.*, vol. 38, no. 1, pp. 526–535, Feb. 2022.

[4] X. An, Y. Cui, H. Sun, Q. Shao, and H. Zhao, "Active-cooling-in-the-loop controller design and implementation for an SMA-driven soft robotic tentacle," *IEEE Trans. Robot.*, vol. 39, no. 3, pp. 2325–2341, Jun. 2023.

[5] P. Wang, Z. Tang, W. Xin, Z. Xie, S. Guo, and C. Laschi, "Design and experimental characterization of a push-pull flexible rod-driven soft-bodied robot," *IEEE Robot. Automat. Lett.*, vol. 7, no. 4, pp. 8933–8940, Oct. 2022.

[6] M. Cianchetti, T. Ranzani, G. Gerboni, I. De Falco, C. Laschi, and A. Menciassi, "Stiff-flop surgical manipulator: Mechanical design and experimental characterization of the single module," in *Proc. IEEE/RSJ Int. Conf. Intell. Robots Syst.*, 2013, pp. 3576–3581.

[7] X. Huang, X. Zhu, and G. Gu, "Kinematic modeling and characterization of soft parallel robots," *IEEE Trans. Robot.*, vol. 38, no. 6, pp. 3792–3806, Dec. 2022.

[8] G. Mengaldo et al., "A concise guide to modelling the physics of embodied intelligence in soft robotics," *Nature Rev. Phys.*, vol. 4, no. 9, pp. 595–610, 2022.

[9] Z. Xie, F. Yuan, Z. Liu, Z. Sun, E. M. Knubben, and L. Wen, "A proprioceptive soft tentacle gripper based on crosswise stretchable sensors," *IEEE/ASME Trans. Mechatron.*, vol. 25, no. 4, pp. 1841–1850, Aug. 2020.

[10] Z. Xie et al., "Octopus-inspired sensorized soft arm for environmental interaction," *Sci. Robot.*, vol. 8, no. 84, 2023, Art. no. eadh7852.

[11] P. Wang et al., "Sensing expectation enables simultaneous proprioception and contact detection in an intelligent soft continuum robot," *Nature Commun.*, vol. 15, no. 1, 2024, Art. no. 9978.

[12] D. Feliu-Talegon, Y. Abdullahi Adamu, A. T. Mathew, A. Y. Alkayas, and F. Renda, "Advancing soft robot proprioception through 6D strain sensors embedding," *Soft. Robot*, vol. 12, no. 4, pp. 465–476, 2025.

[13] C. Armanini, F. Boyer, A. T. Mathew, C. Duriez, and F. Renda, "Soft robots modeling: A structured overview," *IEEE Trans. Robot.*, vol. 39, no. 3, pp. 1728–1748, Jun. 2023.

[14] C. Della Santina, C. Duriez, and D. Rus, "Model-based control of soft robots: A survey of the state of the art and open challenges," *IEEE Control Syst. Mag.*, vol. 43, no. 3, pp. 30–65, Jun. 2023.

[15] D. C. Rucker and R. J. Webster, "Deflection-based force sensing for continuum robots: A probabilistic approach," in *Proc. IEEE/RSJ Int. Conf. Intell. Robots Syst.*, 2011, pp. 3764–3769.

[16] V. Aloi, K. T. Dang, E. J. Barth, and C. Rucker, "Estimating forces along continuum robots," *IEEE Robot. Automat. Lett.*, vol. 7, no. 4, pp. 8877–8884, Oct. 2022.

[17] J. M. Ferguson, D. C. Rucker, and R. J. Webster, "Unified shape and external load state estimation for continuum robots," *IEEE Trans. Robot.*, vol. 40, pp. 1813–1827, 2024.

[18] Q. Qiao, G. Borghesan, J. De Schutter, and E. Vander Poorten, "Force from shape—Estimating the location and magnitude of the external force on flexible instruments," *IEEE Trans. Robot.*, vol. 37, no. 5, pp. 1826–1833, Oct. 2021.

[19] P. Wang, D. Feliu-Talegon, S. Guo, F. Renda, and C. Laschi, "Strain-based modeling of rod-driven soft continuum robots with co-located embedded sensors," in *Proc. IEEE/RSJ Int. Conf. Intell. Robots Syst.*, 2024, pp. 10926–10931.

[20] R. J. Webster III and B. A. Jones, "Design and kinematic modeling of constant curvature continuum robots: A review," *Int. J. Robot. Res.*, vol. 29, no. 13, pp. 1661–1683, 2010.

[21] C. Della Santina, R. K. Katzschmann, A. Bicchi, and D. Rus, "Model-based dynamic feedback control of a planar soft robot: Trajectory tracking and interaction with the environment," *Int. J. Robot. Res.*, vol. 39, no. 4, pp. 490–513, 2020.

[22] A. L. Orekhov, E. Z. Ahronovich, and N. Simaan, "Lie group formulation and sensitivity analysis for shape sensing of variable curvature continuum robots with general string encoder routing," *IEEE Trans. Robot.*, vol. 39, no. 3, pp. 2308–2324, Jun. 2023.

[23] R. L. Truby, C. Della Santina, and D. Rus, "Distributed proprioception of 3D configuration in soft, sensorized robots via deep learning," *IEEE Robot. Automat. Lett.*, vol. 5, no. 2, pp. 3299–3306, Apr. 2020.

[24] C. Della Santina, R. L. Truby, and D. Rus, "Data–driven disturbance observers for estimating external forces on soft robots," *IEEE Robot. Automat. Lett.*, vol. 5, no. 4, pp. 5717–5724, Oct. 2020.

[25] X. Huang, Z. Yuan, X. Yang, and G. Gu, "Precise control of soft robots amidst uncertain environmental contacts and forces," *IEEE Trans. Robot.*, vol. 40, pp. 3565–3580, 2024.

[26] O. Goury and C. Duriez, "Fast, generic, and reliable control and simulation of soft robots using model order reduction," *IEEE Trans. Robot.*, vol. 34, no. 6, pp. 1565–1576, Dec. 2018.

[27] J. Till, V. Aloi, and C. Rucker, "Real-time dynamics of soft and continuum robots based on Cosserat rod models," *Int. J. Robot. Res.*, vol. 38, no. 6, pp. 723–746, 2019.

[28] S. Lilge and J. Burgner-Kahrs, "Kinetostatic modeling of tendon-driven parallel continuum robots," *IEEE Trans. Robot.*, vol. 39, no. 2, pp. 1563–1579, Apr. 2023.

[29] J. Ha, G. Fagogenis, and P. E. Dupont, "Modeling tube clearance and bounding the effect of friction in concentric tube robot kinematics," *IEEE Trans. Robot.*, vol. 35, no. 2, pp. 353–370, Apr. 2019.

[30] A. L. Orekhov, V. A. Aloi, and D. C. Rucker, "Modeling parallel continuum robots with general intermediate constraints," in *Proc. IEEE Int. Conf. Robot. Automat.*, 2017, pp. 6142–6149.

[31] P. Wang, S. Guo, X. Wang, and Y. Wu, "Design and analysis of a novel variable stiffness continuum robot with built-in winding-styled ropes," *IEEE Robot. Automat. Lett.*, vol. 7, no. 3, pp. 6375–6382, Jul. 2022.

[32] F. Boyer, V. Lebastard, F. Candelier, F. Renda, and M. Alamir, "Statics and dynamics of continuum robots based on Cosserat rods and optimal control theories," *IEEE Trans. Robot.*, vol. 39, no. 2, pp. 1544–1562, Apr. 2023.

[33] A. T. Mathew, D. Feliu-Talegon, A. Y. Alkayas, F. Boyer, and F. Renda, "Reduced order modeling of hybrid soft-rigid robots using global, local, and state-dependent strain parameterization," *Int. J. Robot. Res.*, vol. 44, no. 1, pp. 129–154, 2025.

[34] F. Renda, C. Armanini, V. Lebastard, F. Candelier, and F. Boyer, "A geometric variable-strain approach for static modeling of soft manipulators with tendon and fluidic actuation," *IEEE Robot. Automat. Lett.*, vol. 5, no. 3, pp. 4006–4013, Jul. 2020.

[35] F. Boyer, V. Lebastard, F. Candelier, and F. Renda, "Dynamics of continuum and soft robots: A strain parameterization based approach," *IEEE Trans. Robot.*, vol. 37, no. 3, pp. 847–863, Jun. 2021.

[36] K. M. Lynch and F. C. Park, *Modern Robotics: Mechanics, Planning, and Control*. Cambridge U.K.: Cambridge Univ. Press, 2017.

[37] A. T. Mathew, I. B. Hmida, C. Armanini, F. Boyer, and F. Renda, "SoRoSim: A Matlab toolbox for hybrid rigid–soft robots based on the geometric variable-strain approach," *IEEE Robot. Automat. Mag.*, vol. 30, no. 3, pp. 106–122, Sep. 2023.

[38] F. Renda, C. Messer, C. Rucker, and F. Boyer, "A sliding-rod variable-strain model for concentric tube robots," *IEEE Robot. Automat. Lett.*, vol. 6, no. 2, pp. 3451–3458, Apr. 2021.

[39] H. Li, L. Xun, G. Zheng, and F. Renda, "Discrete Cosserat static model-based control of soft manipulator," *IEEE Robot. Automat. Lett.*, vol. 8, no. 3, pp. 1739–1746, Mar. 2023.

[40] F. Renda, A. Mathew, and D. F. Talegon, "Dynamics and control of soft robots with implicit strain parametrization," *IEEE Robot. Automat. Lett.*, vol. 9, no. 3, pp. 2782–2789, Mar. 2024.

[41] A. Y. Alkayas, D. Feliu-Talegon, A. T. Mathew, C. Rucker, and F. Renda, "Shape and tip force estimation of concentric tube robots based on actuation readings alone," in *Proc. IEEE Int. Conf. Soft Robot.*, 2023, pp. 1–8.

[42] Y.-L. Park, B.-R. Chen, and R. J. Wood, "Design and fabrication of soft artificial skin using embedded microchannels and liquid conductors," *IEEE Sensors J.*, vol. 12, no. 8, pp. 2711–2718, Aug. 2012.

[43] C. M. Boutry et al., "A hierarchically patterned, bioinspired e-skin able to detect the direction of applied pressure for robotics," *Sci. Robot.*, vol. 3, no. 24, 2018, Art. no. eaau6914.

[44] T. Jin et al., "Triboelectric nanogenerator sensors for soft robotics aiming at digital twin applications," *Nature Commun.*, vol. 11, no. 1, 2020, Art. no. 5381.

[45] W. Liu et al., "Touchless interactive teaching of soft robots through flexible bimodal sensory interfaces," *Nature Commun.*, vol. 13, no. 1, 2022, Art. no. 5030.

[46] K. Xu and N. Simaan, "An investigation of the intrinsic force sensing capabilities of continuum robots," *IEEE Trans. Robot.*, vol. 24, no. 3, pp. 576–587, Jun. 2008.

[47] R. Yasin and N. Simaan, "Joint-level force sensing for indirect hybrid force/position control of continuum robots with friction," *Int. J. Robot. Res.*, vol. 40, no. 4-5, pp. 764–781, 2021.

[48] R. Xu, A. Yurkewich, and R. V. Patel, "Curvature, torsion, and force sensing in continuum robots using helically wrapped FBG sensors," *IEEE Robot. Automat. Lett.*, vol. 1, no. 2, pp. 1052–1059, Jul. 2016.

[49] F. Khan, R. J. Roesthuis, and S. Misra, "Force sensing in continuum manipulators using fiber Bragg grating sensors," in *Proc. IEEE/RSJ Int. Conf. Intell. Robots Syst.*, 2017, pp. 2531–2536.

[50] A. Gao, N. Liu, M. Shen, M. EMK Abdelaziz, B. Temelkuran, and G.-Z. Yang, "Laser-profiled continuum robot with integrated tension sensing for simultaneous shape and tip force estimation," *Soft Robot.*, vol. 7, no. 4, pp. 421–443, 2020.

[51] D. Feliu-Talegon, A. Y. Alkayas, Y. A. Adamu, A. T. Mathew, and F. Renda, “Actuation reading insights: Estimating shape and forces in tendon-driven slender soft robots,” *IEEE/ASME Trans. Mechatron.*, vol. 30, no. 6, pp. 7878–7888, Dec. 2025. [Online]. Available: https://doi.org/10.1109/TMECH.2025.3581774

[52] C. Y. Wong and W. Suleiman, “Sensor observability analysis for maximizing task-space observability of articulated robots,” *IEEE Trans. Robot.*, vol. 40, pp. 4102–4116, 2024.

[53] T. Yoshikawa, “Manipulability of robotic mechanisms,” *Int. J. Robot. Res.*, vol. 4, no. 2, pp. 3–9, 1985.

[54] N. Jaquier, L. Rozo, D. G. Caldwell, and S. Calinon, “Geometry-aware manipulability learning, tracking, and transfer,” *Int. J. Robot. Res.*, vol. 40, no. 2-3, pp. 624–650, 2021.

[55] C. Zeng, C. Yang, Z. Jin, and J. Zhang, “Hierarchical impedance, force, and manipulability control for robot learning of skills,” *IEEE/ASME Trans. Mechatron.*, vol. 30, no. 3, pp. 1807–1818, Jun. 2025.

[56] I. A. Gravagne and I. D. Walker, “Manipulability, force, and compliance analysis for planar continuum manipulators,” *IEEE Trans. Robot. Automat.*, vol. 18, no. 3, pp. 263–273, Jun. 2002.

[57] G. Smoljkic, D. Reynaerts, J. Vander Sloten, and E. Vander Poorten, “Compliance computation for continuum types of robots,” in *Proc. IEEE RSJ Int. Conf. Intell. Robots Syst.*, 2014, pp. 1066–1073.

[58] M. Bamdad and M. M. Bahri, “Kinematics and manipulability analysis of a highly articulated soft robotic manipulator,” *Robotica*, vol. 37, no. 5, pp. 868–882, 2019.

[59] X. Ma, X. Wang, Z. Zhang, P. Zhu, S. S. Cheng, and K. W. S. Au, “Design and experimental validation of a novel hybrid continuum robot with enhanced dexterity and manipulability in confined space,” *IEEE/ASME Trans. Mechatron.*, vol. 28, no. 4, pp. 1826–1835, Aug. 2023.

[60] D. C. Rucker and R. J. Webster, “Computing Jacobians and compliance matrices for externally loaded continuum robots,” in *Proc. IEEE Int. Conf. Robot. Autom.*, 2011, pp. 945–950.

[61] I. Hussain et al., “Compliant gripper design, prototyping, and modeling using screw theory formulation,” *Int. J. Robot. Res.*, vol. 40, no. 1, pp. 55–71, 2021.

[62] J. Shi, A. Shariati, S.-A. Abad, Y. Liu, J. S. Dai, and H. A. Wurdemann, “Stiffness modelling and analysis of soft fluidic-driven robots using lie theory,” *Int. J. Robot. Res.*, vol. 43, no. 3, pp. 354–384, 2024. [Online]. Available: https://doi.org/10.1177/02783649231200595

[63] R. M. Murray, Z. Li, and S. S. Sastry, *A Mathematical Introduction to Robotic Manipulation*. Boca Raton, FL, USA: CRC Press, 2017.

[64] F. Renda, C. Armanini, A. Mathew, and F. Boyer, “Geometrically-exact inverse kinematic control of soft manipulators with general threadlike actuators’ routing,” *IEEE Robot. Automat. Lett.*, vol. 7, no. 3, pp. 7311–7318, Jul. 2022.

[65] Y. Chen et al., “The SHURUI system: A modular continuum surgical robotic platform for multiport, hybrid-port, and single-port procedures,” *IEEE/ASME Trans. Mechatron.*, vol. 27, no. 5, pp. 3186–3197, Oct. 2022.

[66] Z. Tang, W. Xin, P. Wang, and C. Laschi, “Learning-based control for soft robot–environment interaction with force/position tracking capability,” *Soft Robot.*, vol. 11, no. 5, pp. 767–778, 2024.

[67] H. Yan et al., “Cable-driven continuum robot perception using skin-like hydrogel sensors,” *Adv. Funct. Mater.*, vol. 32, no. 34, 2022, Art. no. 2203241.

[68] Q. Zhao, J. Lai, and H. K. Chu, “Reconstructing external force on the circumferential body of continuum robot with embedded proprioceptive sensors,” *IEEE Trans. Ind. Electron.*, vol. 69, no. 12, pp. 13111–13120, Dec. 2022.

[69] X. An et al., “Shape reconstruction of soft continuum robots via the fusion of local strains and global poses,” *Cell Rep. Phys. Sci.*, vol. 5, no. 10, 2024, Art. no. 102224.

Peiyi Wang (Member, IEEE) received the B.Eng. and Ph.D. degrees in mechatronics and mechanical engineering from Beijing Jiaotong University, Beijing, China, in 2018 and 2024, respectively.

He was a visiting Ph.D. student with the National University of Singapore (NUS) from 2021 to 2023. He was also a Postdoctoral Research Fellow with the NUS. He is currently a Postdoctoral Associate with MIT SMART center, Singapore. His research interests include soft and continuum robotics, human–robot/environment interaction, and robot-assisted or wearable systems.

Daniel Feliu-Talegon (Member, IEEE) received the M.Sc. and Ph.D. degrees in control engineering from the University of Castilla La Mancha, Ciudad Real, Spain, in 2014 and 2019, respectively.

He is currently a Postdoctoral Fellow with the Cognitive Robotics department, Delft University of Technology, Delft, The Netherlands. His research interests include the fractional dynamics and control systems, dynamic control of flexible robots, control of lightweight manipulators in aerial robotics, and sensorization, control, and modeling of soft robot manipulators and deformable objects.

Yuchen Sun has been working toward the Ph.D. degree in mechanical engineering with the Department of Mechanical Engineering, National University of Singapore, Singapore, since 2022.

Her work utilizes first-principles-based mathematical modeling to investigate the mechanics of soft bodies. Her research interests include reduced-order modeling, real-time dynamics, and the integration of mechatronic and software system design for soft robotic applications.

Zhexin Xie (Member, IEEE) received the M.Sc. and Ph.D. degrees in mechatronic engineering from Beihang University, Beijing, China, in 2016 and 2021, respectively.

He was a Postdoctoral Fellow with the Department of Mechanical Engineering, National University of Singapore, from 2022 to 2025. He is currently an Assistant Professor with the Department of Mechanical and Energy Engineering, Southern University of Science and Technology, Shenzhen, China. His research interests include bioinspired robotics, flexible electronics, interactive soft robotic systems, and medical robotics.

Wenci Xin (Member, IEEE) received the B.Eng. degree from the Huazhong University of Science and Technology, Wuhan, China, in 2019, the M.Phil. degree from The Chinese University of Hong Kong, Hong Kong, in 2021, and the Ph.D. degree in Mechanical Engineering from the National University of Singapore, Singapore, in 2025.

He is currently a Postdoctoral Associate with the Singapore–MIT Alliance for Research and Technology (SMART), Singapore. His research interests include bioinspired robotics, soft robotics, soft sensors, and their applications.

Muhammad Sunny Nazeer (Member, IEEE) received the dual master's degree in "European Master's in Advanced Robotics Plus" under the Erasmus Mundus Joint Master's Degree program from Ecole Centrale de Nantes, Nantes, France, in August 2020, and the Ph.D. degree in biorobotics under the Marie Skłodowska-Curie Actions (MSCA) SMART Innovative Training Network from the Department of Excellence in Robotics and AI, BioRobotics Institute, Scuola Superiore Sant'Anna, Pisa, Italy, in March 2024.

Since April 2024, he has been a Postdoctoral Research Fellow with the Soft Robotics Lab, National University of Singapore, Singapore. His current research interests include imitative and adaptive control of self-healing and biodegradable soft robots, and leveraging advanced machine learning paradigms, such as imitation learning, reinforcement learning, and continual reinforcement learning.

Cosimo Della Santina (Senior Member, IEEE) received the Ph.D. degree (*cum laude*) in robotics from the University of Pisa, Pisa, Italy, in 2019.

He was a visiting Ph.D. student and a Postdoc with Computer Science and Artificial Intelligence Laboratory, Massachusetts Institute of Technology, from 2017 to 2019. He was a Senior Postdoc and a Guest Lecturer with the Department of Informatics, Technical University of Munich, Munich, Germany, in 2020 and 2021, respectively. He is currently an Associate Professor with TU Delft, Delft, The Netherlands, and a Research Scientist with German Aerospace Institute (DLR), Munich. His research interests include providing motor intelligence to physical systems, focusing on elastic and soft robots.

Dr. Santina was the recipient of several awards, including the euRobotics Georges Giralt Ph.D. Award in 2020 and the IEEE RAS Early Academic Career Award in 2023. He is involved as a Principal Investigator in a number of European and Dutch Projects, the co-Director of Delft AI Lab SELF, and was the recipient of a NWO VENI.

Cecilia Laschi (Fellow, IEEE) received the graduation degree in computer science from the University of Pisa, Pisa, Italy, the Ph.D. degree in robotics from the University of Genoa, Genoa, Italy, and the Honorary Doctorate degree in bio-inspired robots and soft robotics from the University of Southern Denmark, Odense, Denmark, in 2023.

She was JSPS Visiting Researcher with the Humanoid Robotics Institute, Waseda University, Tokyo, Japan. She is currently the Provost's Chair Professor of robotics with the National University of Singapore, Singapore, leading the Soft Robotics Lab. She is the Director of the Advanced Robotics Centre and Co-Director of CARTIN—Centre for Advanced Robotics Technology and Innovation. She is best-known for her research in soft robotics, an area that she pioneered and contributed to develop at international level. She investigates fundamental challenges for building robots with soft materials, with a bioinspired approach which started with a study of the octopus as a model for robotics. She explores marine applications of soft robots and their use in the biomedical field, with a focus on eldercare.

Dr. Laschi is currently the Editor-in-Chief for *Bioinspiration and Biomimetics*. She founded the IEEE International Conference on Soft Robotics (RoboSoft). She cofounded the spin-off company RoboTech.

Federico Renda (Member, IEEE) received the B.Sc. and M.Sc. degrees in biomedical engineering from the University of Pisa, Pisa, Italy, in 2007 and 2009, respectively, and the Ph.D. degree in biorobotics from the BioRobotics Institute of Scuola Superiore Sant'Anna, Pontedera, Italy, in 2014.

He is currently an Associate Professor with the Department of Mechanical and Nuclear Engineering, Khalifa University, Abu Dhabi, United Arab Emirates. Before joining Khalifa University, he was a Postdoctoral Fellow with the BioRobotics Institute of Scuola Superiore Sant'Anna. He has been a Visiting Professor with the National University of Singapore (NUS), Singapore, the National Institute for Research in Digital Science and Technology (INRIA), Lille, France, and others. His research is applied to the agile motion of highly deformable manipulators as well as underwater swarm robotics for persistent surveillance of large submerged structures. His research interests include the study of multibody dynamical systems, including modeling and control of complex soft and underwater robots.

Dr. Renda has been an Associate Editor and Program Committee Member of important robotics journals and conferences, such as the *International Journal of Robotics Research* (IJRR) and the International Conference on Robotics and Automation (ICRA), to name a few.